

NASA/CR—2003-212179



Doppler Global Velocimetry at NASA Glenn Research Center: System Discussion and Results

Christian T. Lant
Ohio Aerospace Institute, Brook Park, Ohio

February 2003

The NASA STI Program Office . . . in Profile

Since its founding, NASA has been dedicated to the advancement of aeronautics and space science. The NASA Scientific and Technical Information (STI) Program Office plays a key part in helping NASA maintain this important role.

The NASA STI Program Office is operated by Langley Research Center, the Lead Center for NASA's scientific and technical information. The NASA STI Program Office provides access to the NASA STI Database, the largest collection of aeronautical and space science STI in the world. The Program Office is also NASA's institutional mechanism for disseminating the results of its research and development activities. These results are published by NASA in the NASA STI Report Series, which includes the following report types:

- **TECHNICAL PUBLICATION.** Reports of completed research or a major significant phase of research that present the results of NASA programs and include extensive data or theoretical analysis. Includes compilations of significant scientific and technical data and information deemed to be of continuing reference value. NASA's counterpart of peer-reviewed formal professional papers but has less stringent limitations on manuscript length and extent of graphic presentations.
- **TECHNICAL MEMORANDUM.** Scientific and technical findings that are preliminary or of specialized interest, e.g., quick release reports, working papers, and bibliographies that contain minimal annotation. Does not contain extensive analysis.
- **CONTRACTOR REPORT.** Scientific and technical findings by NASA-sponsored contractors and grantees.

- **CONFERENCE PUBLICATION.** Collected papers from scientific and technical conferences, symposia, seminars, or other meetings sponsored or cosponsored by NASA.
- **SPECIAL PUBLICATION.** Scientific, technical, or historical information from NASA programs, projects, and missions, often concerned with subjects having substantial public interest.
- **TECHNICAL TRANSLATION.** English-language translations of foreign scientific and technical material pertinent to NASA's mission.

Specialized services that complement the STI Program Office's diverse offerings include creating custom thesauri, building customized databases, organizing and publishing research results . . . even providing videos.

For more information about the NASA STI Program Office, see the following:

- Access the NASA STI Program Home Page at <http://www.sti.nasa.gov>
- E-mail your question via the Internet to help@sti.nasa.gov
- Fax your question to the NASA Access Help Desk at 301-621-0134
- Telephone the NASA Access Help Desk at 301-621-0390
- Write to:
NASA Access Help Desk
NASA Center for Aerospace Information
7121 Standard Drive
Hanover, MD 21076



Doppler Global Velocimetry at NASA Glenn Research Center: System Discussion and Results

Christian T. Lant
Ohio Aerospace Institute, Brook Park, Ohio

Prepared under Cooperative Agreement NCC3-861

National Aeronautics and
Space Administration

Glenn Research Center

Trade names or manufacturers' names are used in this report for identification only. This usage does not constitute an official endorsement, either expressed or implied, by the National Aeronautics and Space Administration.

The Propulsion and Power Program at
NASA Glenn Research Center sponsored this work.

Available from

NASA Center for Aerospace Information
7121 Standard Drive
Hanover, MD 21076

National Technical Information Service
5285 Port Royal Road
Springfield, VA 22100

Available electronically at <http://gltrs.grc.nasa.gov>

TABLE OF CONTENTS

INTRODUCTION.....	1
DGV TECHNIQUE	2
EXPERIMENTAL SETUP	3
PROCEDURES.....	6
EQUIPMENT LIST	10
FLOW VELOCITY RESULTS	11
WHEEL VELOCITY RESULTS	19
LFM WAVELENGTH CORRECTION & FIBER ILLUMINATION	24
Fiber Bundle Illumination	27
SPECKLE PATTERN MINIMIZATION.....	29
ERROR ANALYSIS.....	32
Possible wavelength calibration errors:.....	34
Calculated Velocity Error.....	35
Speckle Related Error.....	35
CONCLUSIONS.....	38
REFERENCES.....	40
APPENDIX—DIFFERENTIAL VELOCITY PROCESSING	41

INTRODUCTION

The Doppler Global Velocimetry (DGV) measurement system at the NASA Glenn Research Center (GRC) has demonstrated very good quality one-dimensional flow data measurements. The GRC program is a part of a cooperative effort with Langley Research Center (LaRC) to develop a fiber-based beam delivery and image pickup capability for hypersonic propulsion system testing. The GRC effort to date has incorporated LaRC technology to develop and demonstrate the capability to make accurate velocity measurements at supersonic velocities using a fiber optic light sheet delivery system. This report documents the system design, processes, and techniques in an effort to guide future high quality data acquisition.

The data sets highlighted in this report are dubbed “Flow7” and “Cal10” after the parent data directory names in which the image data are stored. The Flow7 data represent velocity measurements from an under-expanded free jet of cold, seeded air in a laboratory environment, where core velocities range from Mach 0.3 to Mach 1.1. The Cal10 data are for a spinning wheel target, which compares the performance of a new fiber bundle illumination beam delivery approach to that of a traditional laser beam propagating in freespace.

Previous results at GRC incrementally improved data acquisition and calibration techniques, developed a robust processing approach, and highlighted both major and minor problems to avoid in the collection of the data. The initial velocity results, achieved taking data from a spinning wheel, were consistent and very useful in debugging the adopted LaRC processing software, but exhibited a proportional calibration error and speckle noise that reduced accuracy and spatial resolution. A simple linear calibration approach (see Appendix) was reasonable for the wheel series of tests, as the range of the Doppler shifts were tuned to fall within the linear region of the absorption line.

An issue that obviated some previous flow test data was that the laser mode-hopping behavior changed since the iodine cell characterizations that were used with the wheel tests. After the wheel tests, the DGV equipment was moved to a different laboratory, and this possibly caused the laser to be disturbed in a way that caused a different number of modes to be skipped at a different region of the operating regime. The ultimate result was that the initial flow tests were conducted with the laser wavelength in a very low sensitivity region of the absorption curve and at a completely different absorption line than expected. In retrospect, some velocities are recoverable from the data, but with very low dynamic range (around 15% of the expected dynamic range). Instead, new data were acquired in which other improvements were implemented.

These issues, and others, were overcome in the subsequent flow testing. The “Flow7” data set reported herein thus benefits from the incremental improvements gained through the learning curve, procedural corrections and improvements in the velocity calculations, and avoidances of unforeseen equipment performance problems.

DGW TECHNIQUE

DGW measurement techniques for various applications have been reported in the literature by a number of researchers, but the GRC program is specifically based on the dynamic velocity measurement approach used by Meyers, et al. at LaRC.¹ In fact, most of the data acquisition system electronics and software used at GRC were designed at LaRC; conversely, the velocity component measurement heads and most of the processing routines reported herein were developed at GRC.

In a simplified overview, the DGW technique is based on the measurement of Doppler shifted narrow band laser light scattered off particles seeding the flow being analyzed. The scattered light is detected by a CCD array camera after being filtered by an iodine vapor absorption cell. The iodine cell attenuates the light as a function of wavelength, which encodes one component of the flow velocity distribution (or Doppler shift distribution) according to light intensity on the camera array. The image is intensity-normalized by an identical camera system by being split before going through the iodine cell – the ratio of the iodine vapor modulated image divided by the unmodulated image gives an intensity-modulated coding of wavelength distributions, corrected for variations in the seed particle scattering cross-section.

Corrections for jitter in the laser wavelength are also performed, by viewing a portion of the illuminating laser beam by an identical two-camera velocity component measurement head. Using four component heads (one for each velocity component and one to monitor the laser wavelength) the three components of velocity can be measured at each pixel over a planar slice of a flow distribution.

The pixel values in each normalized image then represent calibrated optical frequency values converted to velocities in meters per second using the accepted Doppler relationship²

$$\Delta \nu = \frac{\nu_0}{c} (\vec{a} - \vec{l}) \cdot \vec{V} \quad (1)$$

where $\Delta \nu$ is the Doppler-shift frequency difference, ν_0 is the base laser frequency, determined by calibrating the seed laser offset voltage, c is the speed of light, \vec{a} is the unit vector toward the Component camera, \vec{l} is the unit vector of the Poynting vector, and \vec{V} is the velocity vector.

The current system uses two heads to measure one component of velocity, with the system capability to readily add two more components. The DGW measurement advantages are that the measurements are instantaneous over a nine-nanosecond exposure, and have high spatial resolution since each pixel contains all the encoded velocity information at that image location.

EXPERIMENTAL SETUP

The experimental apparatus used to acquire this data is generally the same as for all the flow velocity data runs, as opposed to the markedly different hardware used to generate the previous spinning wheel velocity data. Some changes were made incrementally to the hardware to improve various aspects of the data collection. Among these are: 1. To use an extended nozzle allowing the light sheet and image field of view to get closer to the nozzle exit port (reduces x/D to better understand the flow conditions), 2. to achieve better focusing of the laser light sheet at the test plane, in order to get a thinner planer section of flow data, and 3. to change to non-polarizing attenuators on the Component A head, to avoid scattering-dependent polarization effects. While all of these are thought to have contributed to better data, the successful advances over the flow data runs are primarily due to improvements in test parameter set points (image exposure levels and base laser wavelength selection relative to the absorption lines), iodine cell calibration accuracy, and specific processing algorithms.

The general hardware setup is as follows. The laser light is delivered from the Continuum laser through a Newport high-energy beam attenuator (crossed Glan-Thompson polarizers) via two beamsteering mirrors into a non-imaging multi-mode optical fiber bundle. The fiber bundle output is focused into a light sheet with dimensions approximately 3 x 25 mm at the test section. Lower intensity marginal light is blocked with an adjustable slit aperture to provide better width definition to the sheet. See Figure 1 for a picture of the test section.

A 0.1% portion of the beam is split after the fiber to a ground screen, onto which the Laser Frequency Monitor (LFM) head is focused at near-normal incidence. The split is accomplished with a custom beam sampling cube fabricated by CVI Laser Corp, whose specifications are shown in Figure 2.

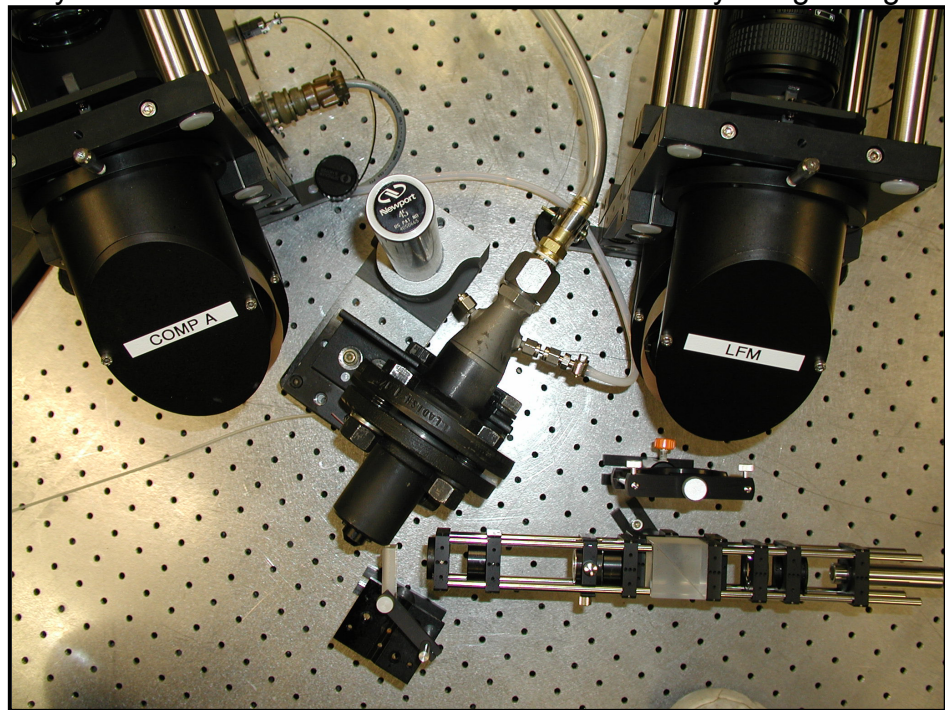


Figure 1: Test section showing free jet nozzle, Component A and LFM heads, and fiber bundle/beam splitter/light sheet generator. Tapped holes in optical table are on 1" centers.

The two frequency measuring component heads are now of the same design, with the sole difference being the use of crossed polarizers in the LFM to adjust the signal

levels between the reference and signal cameras. The overall signal level on the LFM cameras is adjusted by a stack of neutral density filters placed in front of the LFM beamsplitter. The Component A head has been retrofitted with neutral density filters to adjust the relative intensities between the reference and signal camera, on the caution that the scattering properties of the seed particles may change the calibrated ratios. Conversely, the LFM uses the same ground screen for both the calibration and the measurement runs, and is assumed not to be dependent on polarization.

Previous tests showed no spatial dependence on frequency of the image ratios, so the LFM correction uses the average value of the pixel ratios to correct the

Doppler shifted frequency measurement. Although there has been observed slight trends and noise on zero velocity images, these have also been observed in the flat field images at the same magnitude and thereby are not attributed to a spatial wavelength distribution in the laser beam.

The flow that is being measured is generated by a converging nozzle of cold air seeded with an olive oil aerosol. The nozzle outlet diameter is 3/8". The plenum pressure is monitored via a tap connecting the plenum to a TBD absolute pressure gauge. The flow is underexpanded, and is generated by plenum pressures ranging from 15 to 30.8 psia.

The test geometry for this run can be seen in Figure 3. The light sheet is incident at 59° from the flow direction toward the right of the page, and the Component A field of view is oriented at -55° from the flow direction. The velocity component measured is then about 2° off of the negative flow direction, along a unitless "sensitivity vector" **R**:

$$\begin{aligned} \mathbf{R} &= (\mathbf{a} \cdot \mathbf{I}) = -\cos(59^\circ) \cdot \cos(55^\circ) \\ &= -1.09 \end{aligned} \quad (2)$$

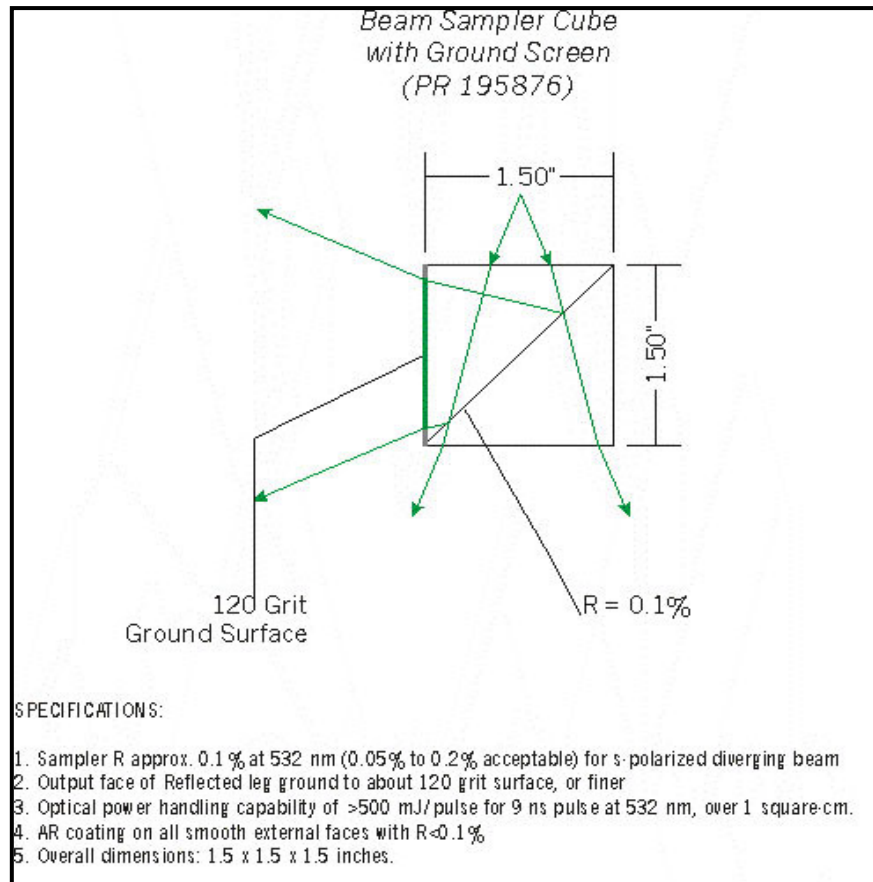


Figure 2: Specifications for custom beam sampler cube with ground screen.

where \mathbf{a} is the unit vector in the direction of the camera, and \mathbf{l} is the unit vector from the laser. The laser sheet slices the flow at an x/D of about 1 to 2, and passes through the center of the core flow at about $x/D = 1.7$.

The view of each data image shows the left boundary of the data, which is defined by the last column of dots visible before being occluded by the nozzle edge. Referring to the figure, the illuminated region of the flow is the intersection of the green laser sheet with the light gray FOV arrow for Component A. Starting from the left edge, the flow regions represented in the data images, therefore, integrate the velocities from: 1. The mixing region at around $x/D=1.2$; 2. the core region at around $x/D=1.7$; and 3. the down-stream mixing region at around $x/D=2$ to 2.5. The data boundaries of the mixing regions are determined by the signal level arising from the amount of seed that is drawn in from the core flow. The constant velocity core region is approximated by the cone drawn to converge at a point around four nozzle diameters from the nozzle exit.

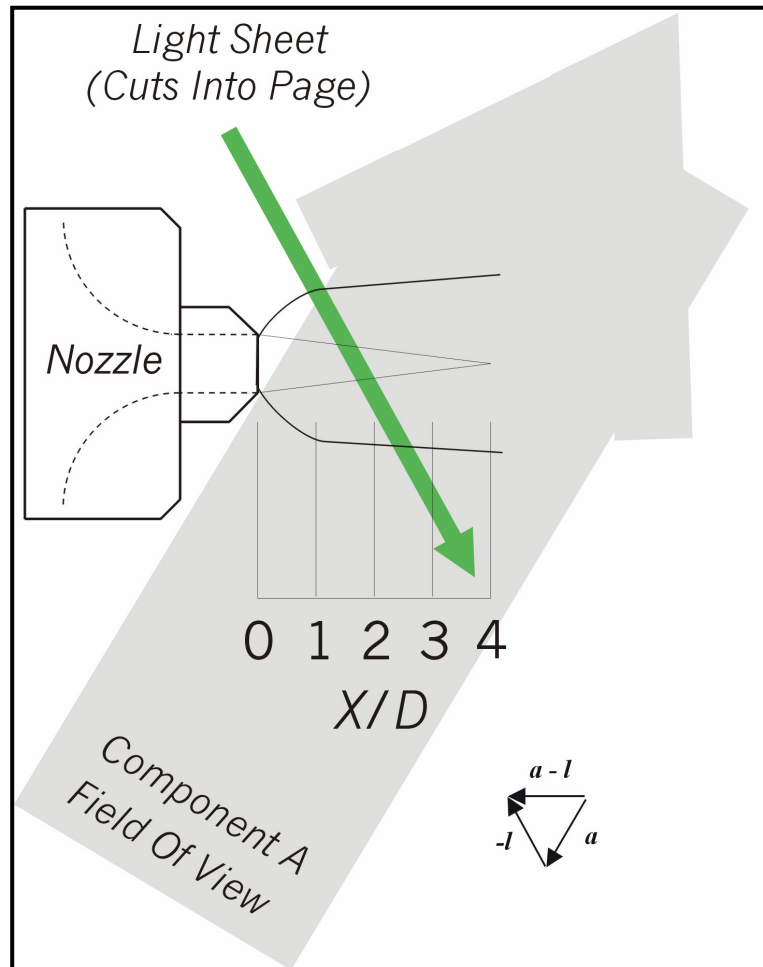


Figure 3: Scale diagram showing test geometry and flow measurement orientations. The nozzle diameter is $3/8$ ", and the sensitive velocity component is indicated by vector $(\mathbf{a} - \mathbf{l})$.

PROCEDURES

The iodine cells were set with the finger temperatures at 55 °C using the Iomega PID temperature controllers. This put the body temperature of the cells at around 71 °C. The transmission characteristics of the two cells were then measured after setting the camera attenuation levels to those needed during the laser exposure of the velocity tests. This exposure ratio setting is a compromise to maximize the dynamic range of the laser exposures without saturating pixels, while also guaranteeing successful centroid processing of the white light illuminated dot card images. The difficulty mostly comes from the need to use the reference/signal beamsplitter coating for both 532 nm and white light exposures, as the transmission/reflection ratio is different for each illumination source. In addition, the signal level from each target is different (ground glass, seeded flow, dot card), so adjustability, using stacks of various neutral density filters, is provided for each camera as well as for each component.

Since the ratios are tuned to optimize the camera exposures at 532 nm, the proper exposure (brightness, flatness, and contrast) of the dot card images is achieved digitally off-line. This is important, as the success of the centroid processing is very sensitive to correct exposure and processing settings. However, the traditionally preferred approach of adjusting the exposure at the camera could not be done reliably without altering the calibration data. The current setup helps by using a wideband green transmission filter over the white light sources, but the camera image split ratio is still not near 50% (as with the 532 nm illumination) and digital adjustments are needed.

To calibrate the I_2 cells, the injection seed laser thermoelectric cooler's drive voltage was varied between -4.0 to 10.0 volts for a coarse characterization. After observing different mode hopping behavior of the Nd:YAG laser than at the previous calibration, a finer calibration was done over the desired range of interest of -2.00 to 1.00 volts. The negative slope of the $18,789.98\text{ cm}^{-1}$ (532.1986 nm) I_2 absorption line was then chosen for the current DGV test geometry for a number of reasons: 1. the negative slope compensates for the signal loss due to decreasing seed density at increasing velocities, by attenuating the red-shifted laser light less as the velocity increases; 2. the transmission dynamic range of this line for these I_2 cells is greater than the neighboring lines; 3. no mode hopping behavior is observed in the laser operating region of this line.

Figure 4 shows the I_2 cells' transmittance data over the selected absorption line, as a function of the seed laser's wavelength control voltage. The calibration data were converted to a look-up table (LUT) for each component, which converted the normalized transmission ratios to absolute laser wavelengths. The LUTs were organized to associate gray scale values of 1 to 512 with wavelengths ranging over the negative-slope region of the absorption curve. Data points describing the absorption curve were interpolated using Origin 6.1 software to generate a final ASCII file of integer gray scale values and their associated wavelengths. These data sets are shown in Figure 5.

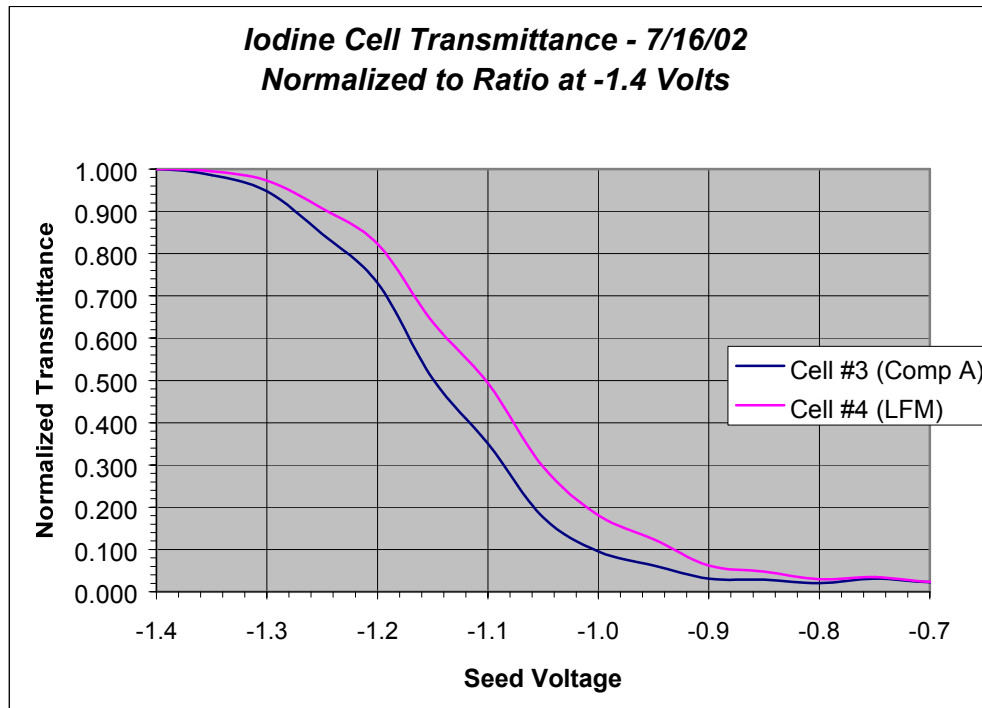


Figure 4: Transmittance data over the absorption line used to acquire the test data, normalized to the flat field ratio at -1.4 V. The primary seed laser offset voltage was -1.0 V.

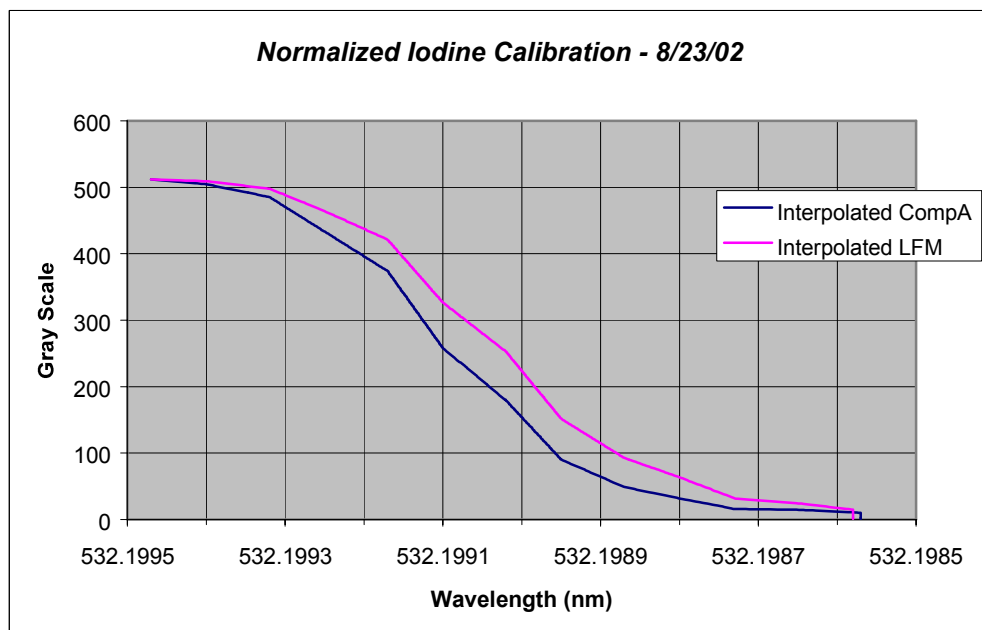


Figure 5: Iodine cell calibration data after conversion to LUT format. Integer values of 1 to 512 map to transmission values normalized to the flat field voltage ratio.

The Flow7 data were processed using the absolute frequency measurement technique described below. This procedure to relate the velocity image ratio data to the calibration data involves normalizing the calibration data by the calibration flat field wavelength transmission ratio, and later normalizing the velocity data by the most recent test flat field transmission ratio. This partially corrects for environmental changes in the transmission characteristics since the last calibration. Each normalized pixel ratio value can then be assigned a calibrated wavelength, which can then be converted to velocity using the geometrical constants measured during the set up.

The procedure to prepare the wavelength calibration LUTs follows:

1. Acquire image pairs for each component head, sequentially over a range of seed laser offset voltages. Acquire twenty image pairs to average for each head at each offset voltage.
2. Cross-correlate image pairs, correct offsets, calculate ratios according to the equation:

$$ratio(i, j) = 512 \cdot \left[\frac{signal(i, j)}{reference(i, j)} \right] \quad (3)$$

3. Perform averaging over a representative ROI for each component:
 - a. Calculate ratio pixel means and s.d. over twenty images (temporal pixel means)
 - b. Calculate spatial mean and s.d. of temporal pixel means over ROI
 - c. Record a single spatial-temporal mean value for each component at each offset voltage.
4. Normalize these ratios by the ratio (peak) found at the flat field voltage selected for this line, according to

$$Normalizedratio(i, j) = 512 \cdot \left[\frac{Ratio(i, j)}{FlatfieldRatio} \right] \quad (4)$$

5. Interpolate these curves to generate wavelengths at integer values of gray scale from 1 to 512.
6. Store in the format: (Gray Scale, CompA Wavelength, LFM Wavelength). This comprises the LUT for this calibration run.

The procedure to measure velocity at each pixel is then to:

1. Acquire all background, flat field, and velocity data.
2. Subtract the average raw background image from each raw reference and signal image.
3. Dewarp (and further align by correlation, if needed) each image pair for the LFM and CompA images.
4. Take the image ratios using the IDL ratio script, according to Equation 3.
5. Take flat field temporal and spatial mean for CompA and LFM. Store in velocity set file for calibration ratio normalization.
6. Convert each array of pixel ratios to wavelengths using the calibration LUTs.
7. Calculate the velocities at each pixel using the Doppler wavelength and LFM wavelength calculated in step 4, and the geometric sensitivity vector from Equation 2.

The data were collected using version 5 of the LaRC DGVAck32.exe and the corresponding version of the DGVRec.exe software. The signal split between each pair of component cameras was adjusted by acquiring a set of image pairs and viewing them with a pixel-interrogating viewer (University of Texas' ImageTool). The images were adjusted so that the relevant regions of interest were below saturation with the laser set at the flat field frequency.

EQUIPMENT LIST

The following lists major equipment used in the system.

1. Pulsed, doubled, injection-seeded Nd:YAG laser; Continuum NY82S-10
2. Fiber optic bundle with circular input and output apertures, 2 m; CeramOptek P/N PLGSS2/UV200/8.0MM/BPGS/2.0M/NASAG
3. Custom beamsplitter cube with ground output face; CVI P/N PCB-532-0.1-150-S-UV/FG
4. Iodine cells #3 and #4 (CompA and LFM, respectively)
5. 3/8" diameter free jet; NASA GRC fabrication, with protruding tip
6. Seed generator with olive oil aerosol; TSI six jet atomizer
7. CCD array cameras; Hitachi KP-F1, analog, 640 x 480 pixels
8. 8-bit ADC framegrabbers; Matrox Pulsar
9. DGVEMS timing generator; NASA LaRC fabrication
10. Four Channel Delay/Pulse generator; Stanford Research Systems Model DG535
11. Absolute gas pressure gauge; Heise Model 710B
12. Dot card grids: LFM \Rightarrow 5/16" dot pitch; CompA \Rightarrow 1/2" dot pitch
13. DGVAcq32 Acquisition and receiver software; NASA LaRC version 5 (Jan, 2000 load)

FLOW VELOCITY RESULTS

Two runs of data were collected in the course of this flow test. The first one was collected with a seed laser offset voltage of -1.0 volts, and the second was collected with a seed laser offset voltage of -1.1 volts. For this test, the goal in selecting the offset voltage was to maximize the velocity range while not losing too much sensitivity near the lower-sloped ends of the absorption line. The base wavelength must not be at a maximum or a minimum of the absorption curve, even if all the measured velocities are expected to be non-zero, as the LFM always operates immediately around this base wavelength. The data set using an offset voltage of -1.1 volts was taken as a contingency, in case the data set using an offset voltage of -1.0 volt was found to have too much noise (in hindsight, it didn't; but it did prove to be useful comparison data).

Figure 6 shows an instantaneous image of color-coded velocity measurements for a pressure ratio of 0.937. The color scale was chosen to cover the velocity range in the series of images without saturation. The pixel values represent calibrated optical frequency values converted to velocities in meters-per-second, using the standard Doppler relationship given in Equation 1. The orange halo represents where the seed density and/or the illumination level falls off such that either the reference or signal image intensity is very low (also see the Error Analysis section). Since the flow was seeded in the core within the plenum, the transition boundary region is poorly seeded, with signal only available where seed has moved from the core. A vertical slice through any horizontal point in the image represents a constant x/D .

The velocity images were subsequently masked by an image generated by a reference image thresholded at a gray scale value of 10. This subjective threshold seems to eliminate most of what is considered noise in the following

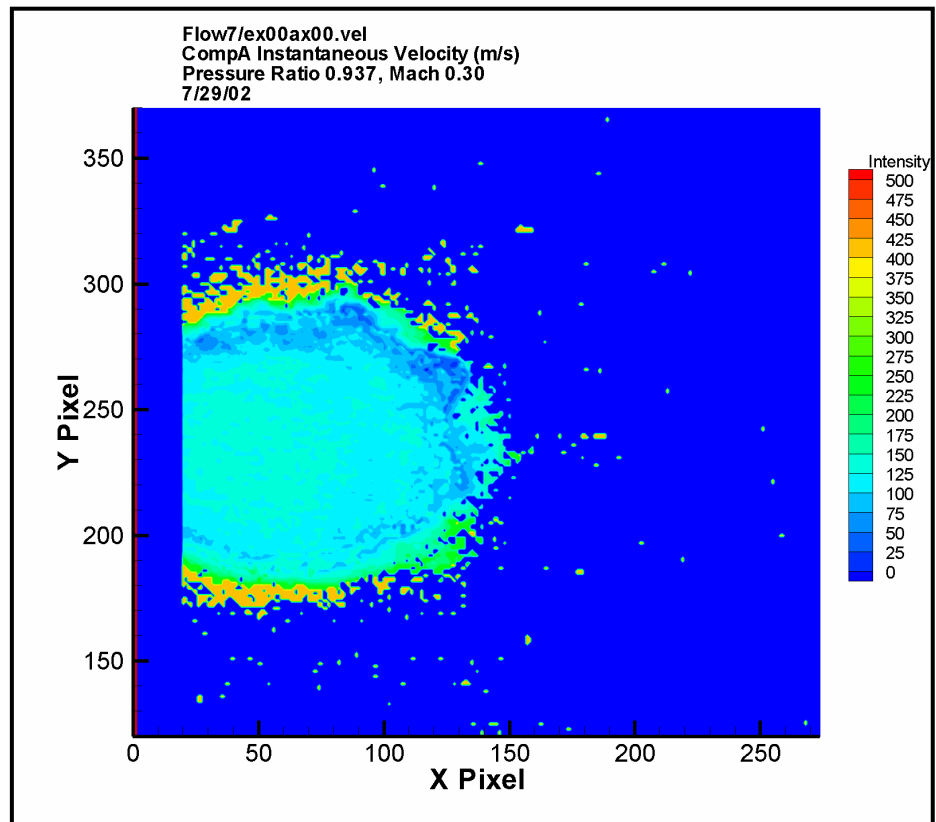


Figure 6: Instantaneous velocity map of flow at a pressure ratio of 0.937. Color coded velocities are in m/s. The core flow is centered approximately about pixel (65,244)

data. A side effect is that the mask can also show where the core boundary is on the right side of the images. It is preferable to generate the mask based on the reference image, which give the best information on where the flow is well seeded (or illuminated) and where it is not. A drawback with this approach is that, depending on the signal level, this threshold will typically allow some noisy data to remain or, conversely, mask some meaningful data. Currently, a mask is generated from the

first image in the series, which for turbulent flow has

a unique seed boundary; averaging a series of images, in this simple algorithm, necessarily excludes regions having data in other images and includes regions that should be masked in other images. These overlapping mask regions are thus not weighted properly in the averaged images. These overlapping mask regions are thus not weighted properly in the averaged images.

Alternatives would be to 1. logically AND the masks to generate a common mask, or 2. normalize each pixel by the number of mask which include said pixel.

Alternative '2' would be preferable, as it includes the

most data in the final result (albeit not all averaged resulting pixels would have undergone the same

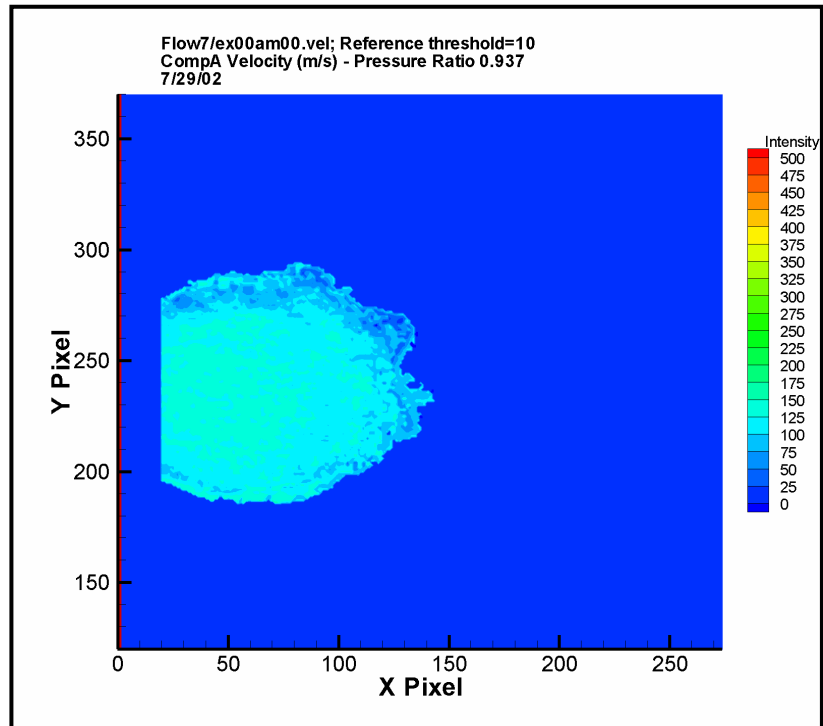


Figure 7: Same data as figure 6, but with a threshold of 10 applied to the reference image to mask the noise region.

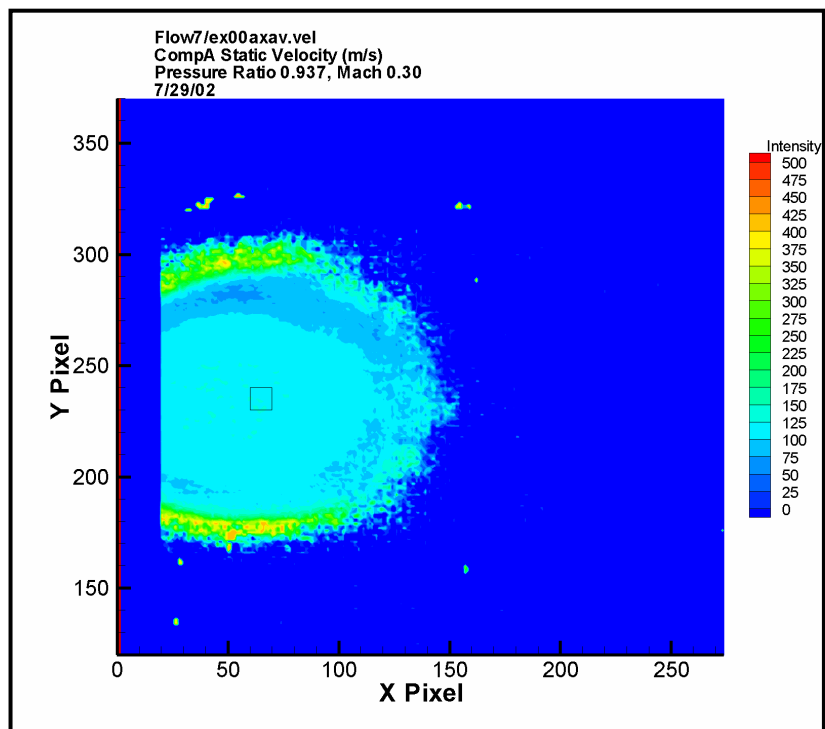


Figure 8: Flow data averaged over ten images, for Mach 0.3 core flow. The box outline represents core flow ROI in later plots. The green halo indicates the noise floor as the scattering intensity drops off.

number of samples).

Figure 7 shows the same data as in Figure 6, only being masked as initially described above. The image shows a central region having velocities ranging from 100 to 140 m/s, with an average value of 121 m/s.

A ten-image average of data taken at a pressure ratio of 0.937 is shown in Figure 8, with a 10 x 10 pixel ROI shown as a black outline. This ROI is later used to calculate a representative core velocity. This ROI is centered around pixel (65,235), which is felt to be close to the flow centerline, based on image symmetry. A relatively large ROI previously extended across the core flow region to the mixing regions at the outer radii; although this larger ROI better represented the average velocity in the image, it did not represent the core velocity for which accurate comparison velocities can be calculated. The smaller core region was therefore used in the later comparison plots.

Figure 9 shows an image of instantaneous velocities at a plenum pressure ratio of 0.474. As in Figure 6, the orange halo represents a region of very dim intensity and is considered noise. The core flow region seems to

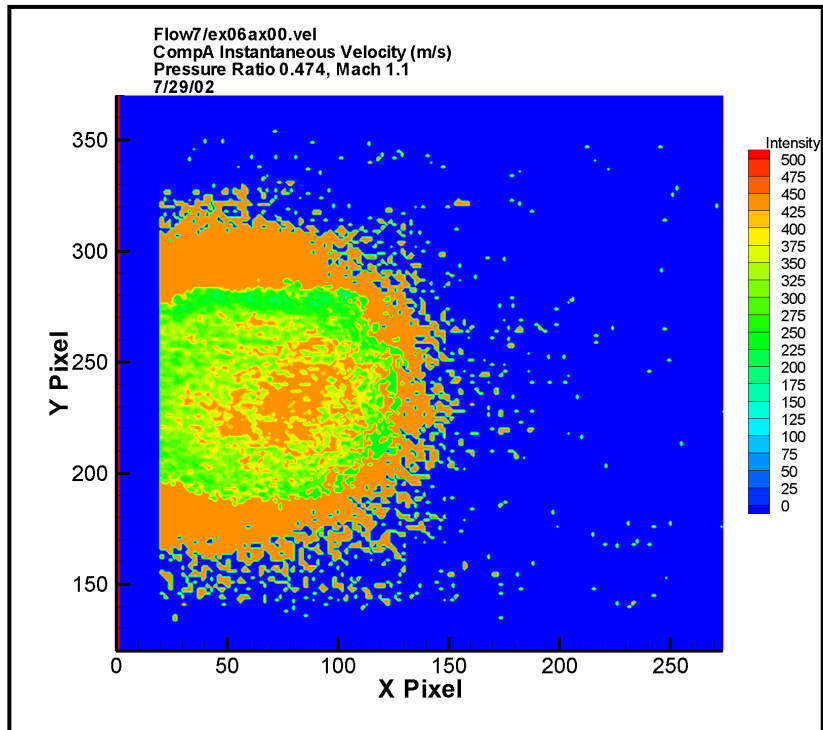


Figure 9: Instantaneous velocity map of flow at a pressure ratio of 0.474. Core flow velocity is calculated to be Mach 1.1. The core flow is centered approximately about pixel (75,235)

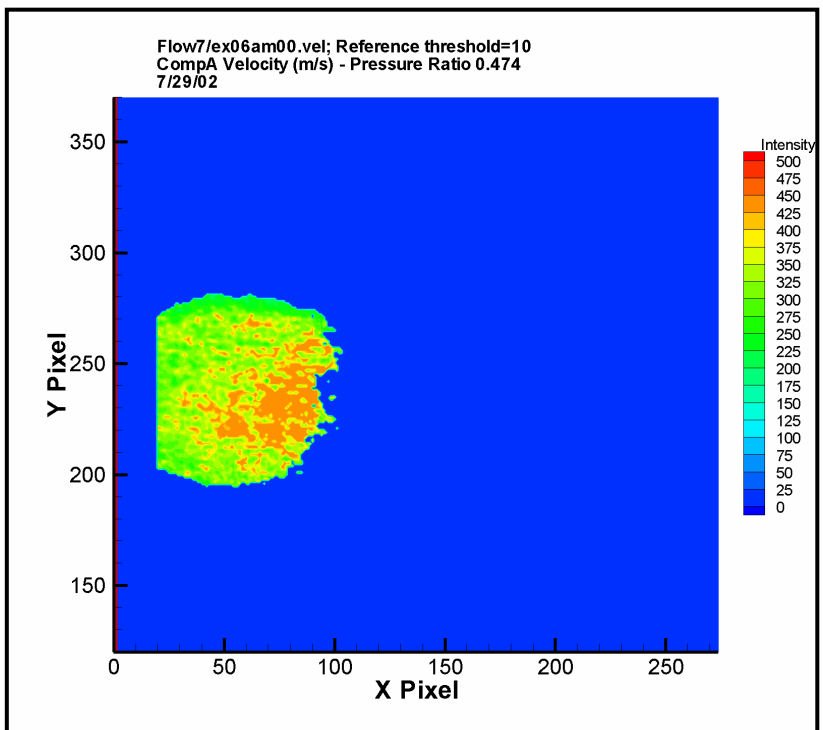


Figure 10: Same Mach 1.1 data as in Figure 9, but with a threshold of 10 applied to the reference image to mask the noise region. The threshold appears to have removed some real low-signal data to the right of the core region.

be centered around pixel (70,235) in this image. Figure 10 is the same data, but masked using an image generated by thresholding the reference image with a value of 10; the two images show that the threshold value must be selected carefully so as not to mask possibly significant data.

Figure 11 shows a ten-image average at a pressure ratio of 0.474, with an 80 x 60 pixel ROI and a 10 x 10 pixel ROI shown as black outlines. Again, the smaller ROI is later used to calculate a representative average velocity.

Figure 12 is a sequential view of the series of increasing velocity data. The images each represent an instantaneous map of velocities, masked to remove the noise background. The box outlines represent the same 10 x 10 pixel region-of-interest used to determine the core velocities for subsequent plots. The same threshold value of ten is used on all the plots, which leads to variations in the usable data areas. The thresholds can be refined by hand, but has not been done here in the interest of uniformity.

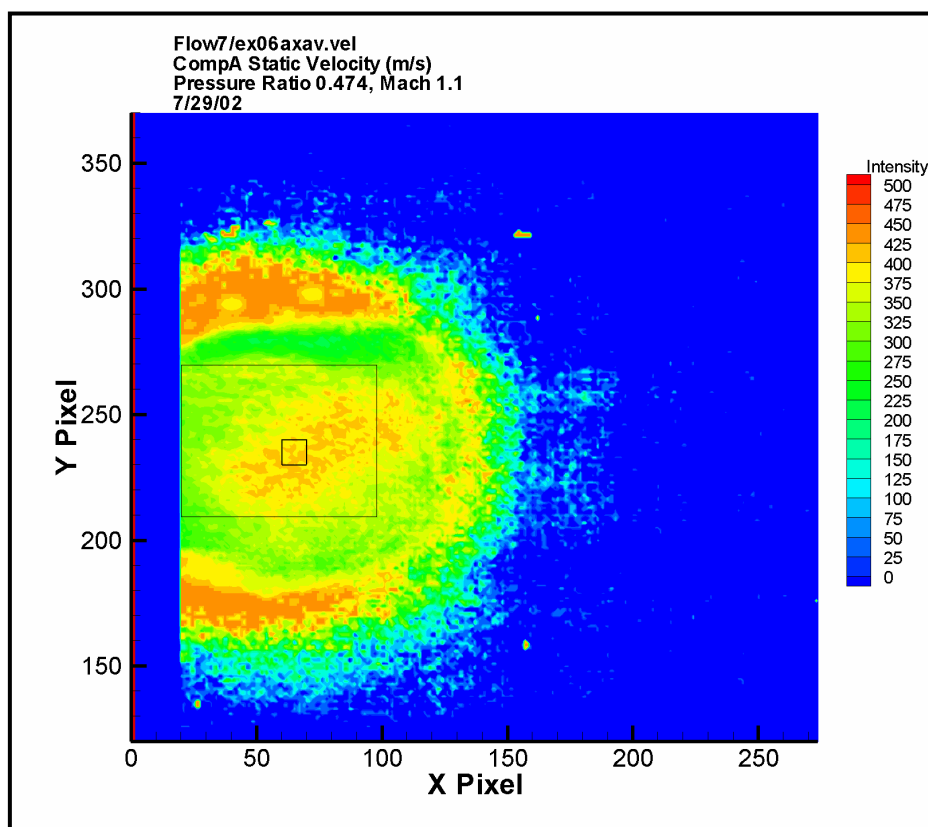


Figure 11: Flow data averaged over ten images, for Mach 1.1 core flow. Box outlines represent core flow and image mean ROI data shown in later figures. The orange halo represents noise.

The data are averaged temporally and spatially to determine a representative velocity measured at each plenum pressure ratio. These local averages are calculated as follows. Each image is processed to yield pixel values of instantaneous velocity, and a series of ten such images taken at ten pulses of the laser yield the temporal velocity average at each pixel. A spatial average is then taken over a region of interest (ROI) in each of these average images, and plotted in Figure 13 for each set of data taken at a different pressure ratio.

Figure 13 then shows plots of the measured velocities versus the expected velocities. The expected velocity is shown in green with a slope of unity, against which the measured velocities are compared. The calculated velocities came from a table generated by NASA Ames Research Center³. The data taken at an offset voltage of

-1.00 V, representing data sets “ex00” through “ex07”, are shown in blue; the data taken at an offset voltage of -1.10 V, representing data sets “ex10” through “ex16” are shown in red. The averages represented by the blue line and the red line use a very small ROI of 10 x 10 pixels, in order to sample the core region of the flow. Previous ROIs of 80 x 60 (4,800) pixels, and 50 x 10 (500) pixels show very similar trends in the data and similar standard deviations, however, the slopes are lower (slightly higher than unity). Table 1 shows the statistics of these fits.

The trends given by the core flow ROI averages give slopes of about 1.10 and 1.32, but with similar profiles. The last three data points on the red line show a flattening or clipping of the measured velocity, which is due to the Doppler shifts pushing the wavelength into the transmitting region of the absorption line. These three points are, therefore, not included in the linear fit.

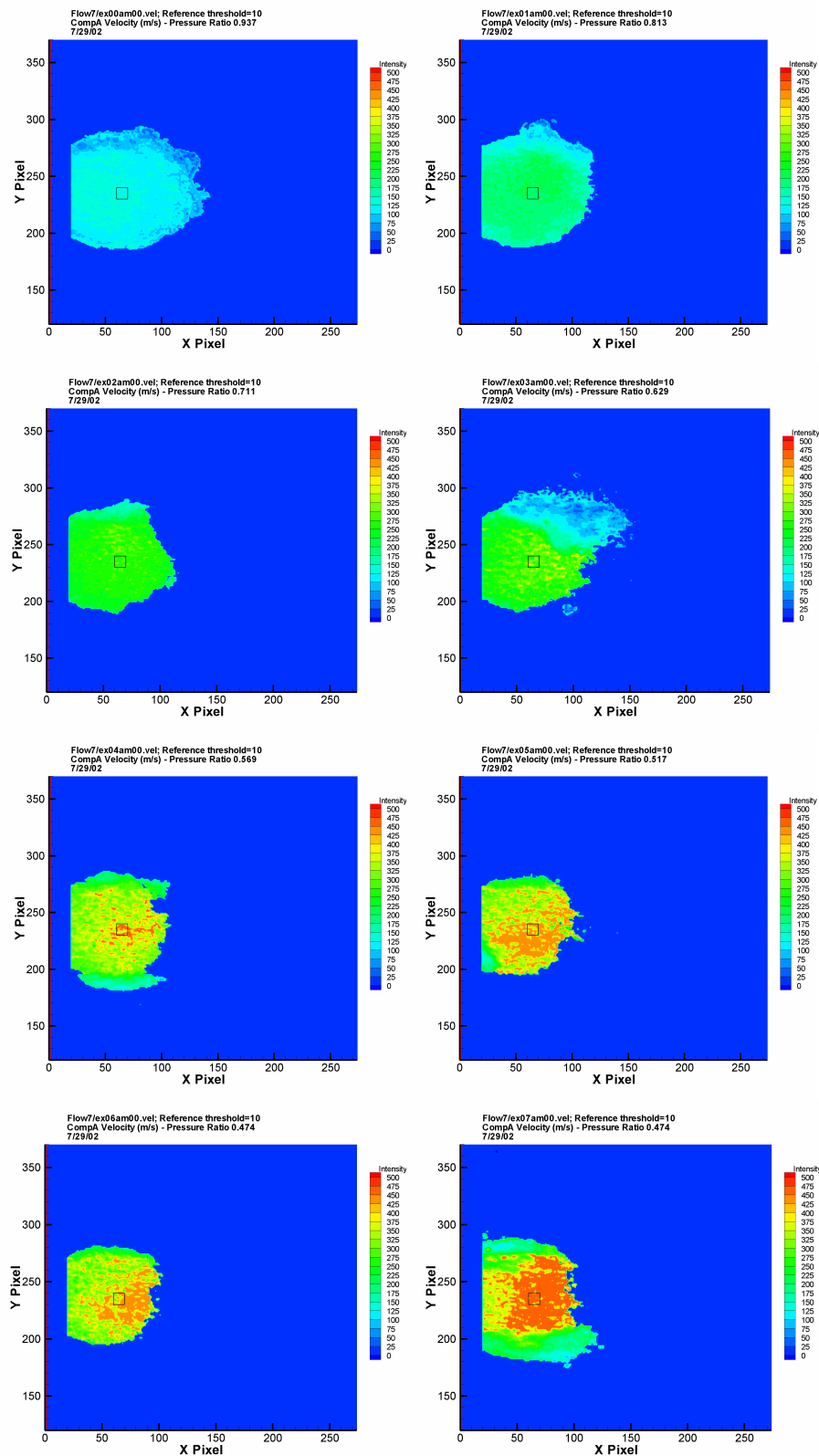


Figure 12: Series of eight instantaneous flow images for increasing pressure ratios (series ex00 through ex07). Mach number increases from left to right, and top to bottom. Box outline indicates ROI for core velocity plot.

The core velocity should be constant over a converging cone reaching from the nozzle exit to a point roughly four nozzle diameters downstream. The ROI used in the above plots are $\pm 5 \times 5$ pixels centered about pixel (65,235) for the core region. The agreement between the two runs at different seed voltages is excellent, up to the region where clipping occurred in the 1.1 V run; the error bars, representing Table 5, show that each velocity point agrees to within the theoretical resolution of the measurement, and all but one measurement point agrees to within the theoretical uncertainty with the expected velocity. The data above 200 m/s in both runs, however, seem to deviate much more from the theoretical velocity predicted by the nozzle pressure ratio. This profile is seen over a variety of different conditions, which tends to discount most systematic errors: different absorption region, slightly different nozzle pressure settings (pressure set points differed by 0.1 psi), and different spatial averaging ROIs (discounts local steady state flow variation).

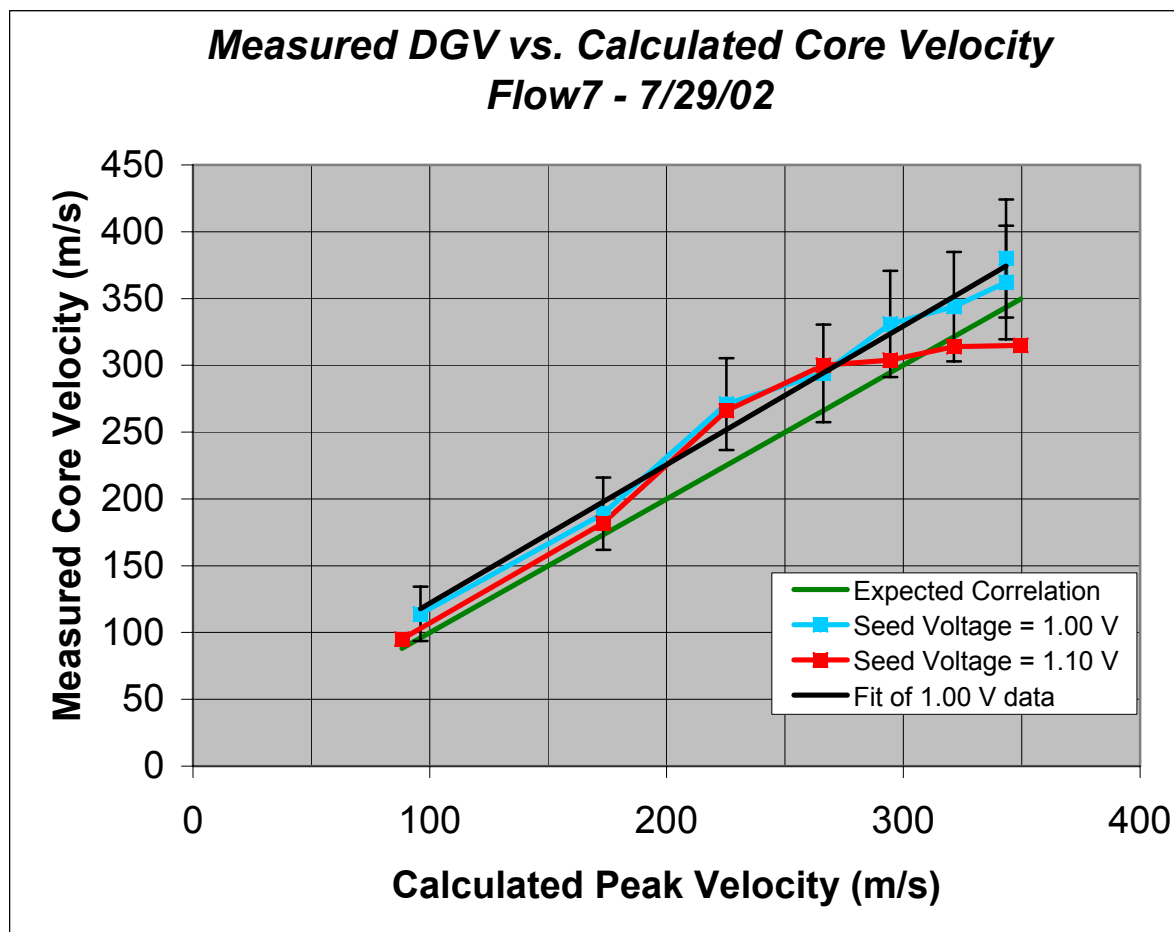


Figure 13: Comparison plots between measured and calculated core flow velocities. The blue line has a slope of 1.1 and an offset of 20 m/s. The black line is a linear fit with these coefficients. The green line is the expected correlation with a slope of unity. The error bars on the blue line show all but one data point to be within the theoretical uncertainty. The red line, which is included to show repeatability, is a second run through the same pressure ratios, but with a seed laser offset of 1.10 V, which puts the center wavelength more toward the middle of the iodine absorption line; the data was subsequently shifted into the flat transmitting region of the line, so the last three data points are invalid.

A likely remaining error is in the plenum pressure measurement. For example, a leak in the pressure tap tubing may become significant above a pressure of 20 psi, leading to higher actual velocities at the nozzle. A post-test calibration of the pressure gauge and tap indeed showed small leaks in the tubing and the swedge tubing fitting, but an accurate correction calibration was not possible, since the fittings were tightened prior to the calibration.

Figure 14 shows slices of data taken across each velocity data average image, for each pressure ratio. The slices are taken at pixel row 240, which may be slightly higher than the flow axis around pixel 235. Referring to the geometry shown in Figure 3, each slice in Figure 14 consists of a central core region surrounded by mixing regions on the left and right; the plots cover flows from one to two nozzle diameters as the pixel number increases from left to right. The grayed-out box with the dashed outline indicates a region of low signal level due to low seed concentration for the higher velocity runs ex04, ex05, and ex06.

The expected profile at each pressure ratio is a flat velocity profile in the core flow region included between pixels 60 to 80, which falls off to the ambient air velocity (zero, in this case) at each radial extreme (this extreme is well out of the range of the current data, as the data are limited to the seeded region).

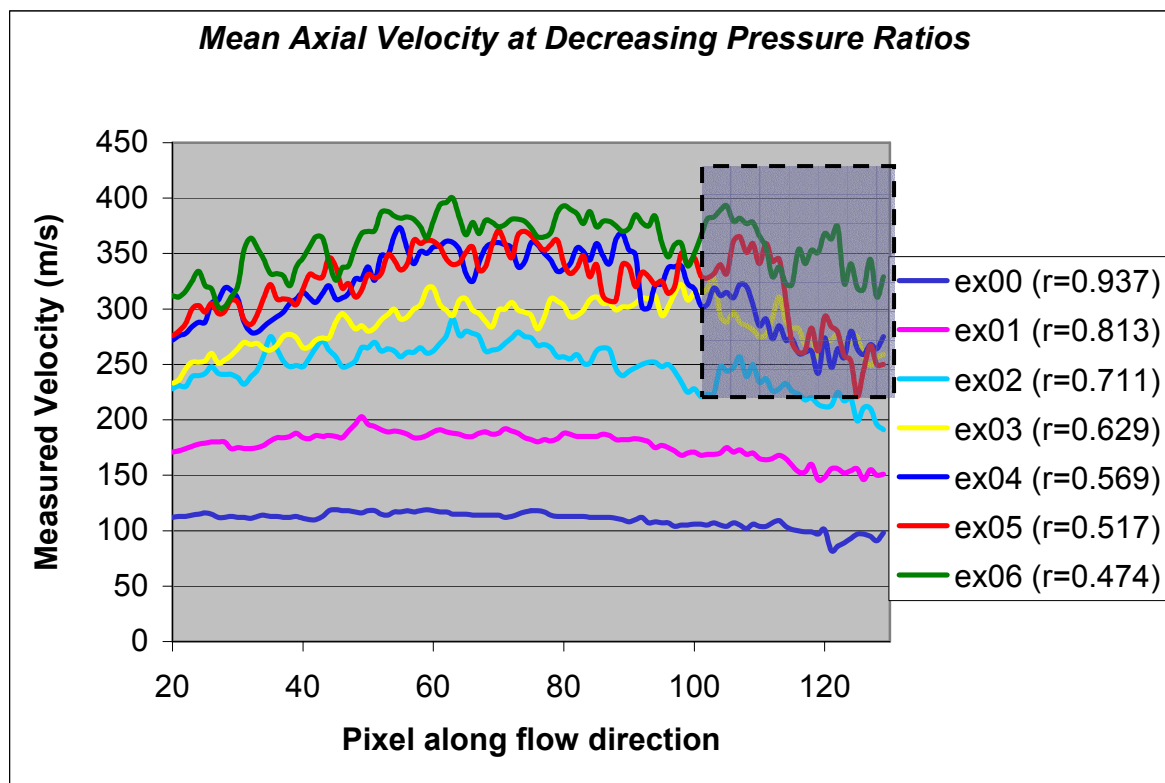


Figure 14: Mean velocity slices for increasing pressure ratios. Roll-offs at the ends indicate the transition flow regions. A slight asymmetry indicates the varying x/D and a restricted FOV on the left sides of the images. The core region is included between pixels 60 to 80. Significant signal drop-off is typically observed at pixel numbers above 110. The grayed-out region within the dashed outline indicates very low signal levels in the higher speed data. They are included here because they follow the expected trend, however, there seem to be discontinuous jumps in the ex04, ex05, and ex06 data.

WHEEL VELOCITY RESULTS

A standard test application for DGV measurements has been to measure the velocity distribution on a spinning wheel covered in fine grit sandpaper. This test was performed at GRC with the two-fold goal of demonstrating basic velocity measurements and comparing results using wheel illumination via a fiber bundle versus freespace beam propagation. The following results were observed.

Data were acquired using a 11.8" diameter wheel spinning at 3,000 RPM, as measured with a Hall effect sensor on the wheel mount. The setup was designed to measure the horizontal component of velocity. The data were processed according to the differential technique described in the Appendix. Taking into account the geometric sensitivity vector $\mathbf{a} \cdot \mathbf{l}$, the calculated component of the measured wheel rim speed is ± 33.3 m/s.

Figures 15 and 16 show masked single image results of the wheel velocity distributions, using a smoothing kernel of 1 and 11, respectively. The velocities are color coded with an offset of 1000 m/s to avoid negative numbers in the scaling. The figures show a progressive horizontal velocity increasing from top to bottom of the wheel, which spins counter-clockwise. Figure 16 adds smoothing by an 11x11 kernel, to reduce noise from speckle variations. Slices of these two images are shown as the purple data in Figures 18 and 20.

A comparison between the fiber-delivered illumination and the freespace propagating illumination is seen in Figure 17. After spatially smoothing the image with an 11x11 kernel to compensate for speckle variations, the measured rim speed values range from 33 to -47 m/s for the fiber illumination data and 18 to -38 m/s for the freespace beam illumination data, and are plotted in red and yellow, respectively, in Figure 17. The green line indicates the calculated values expected for the given setup, and the red line is a linear fit of the fiber data. The standard deviation from a linear fit through each set of data is 4.1 m/s and 9.4 m/s for the fiber and freespace illumination cases, respectively. Both data sets are a single pixel column from a spatially smoothed instantaneous image of velocity data, normal to the sensitive axis.

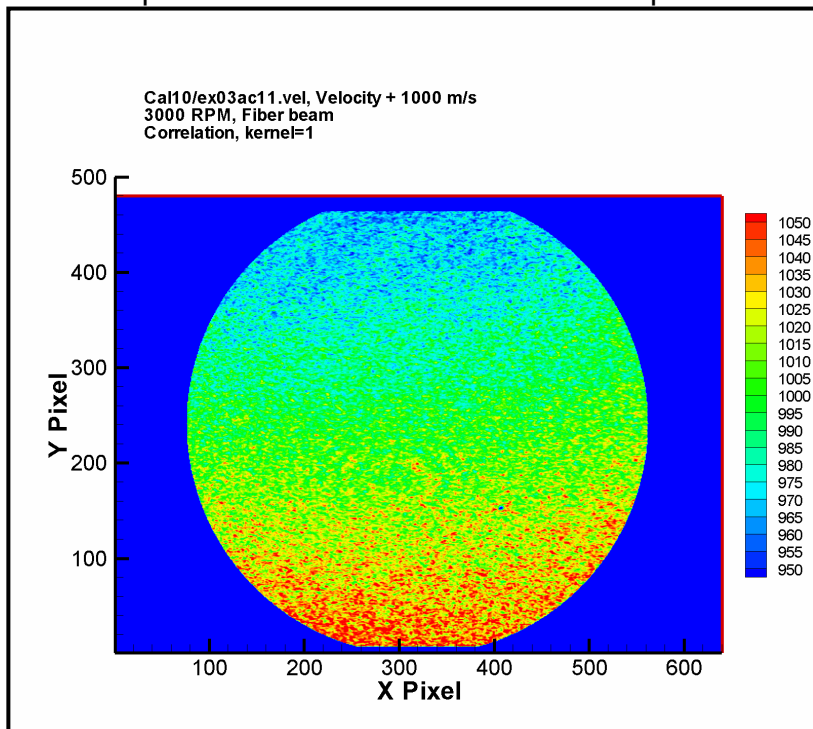


Figure 15: Single image of velocities measured for a wheel spinning at 3000 RPM. The wheel is fiber-illuminated, the reference and signal images are aligned by cross-correlation, and the ratios are not smoothed.

The “random” noise visible in the data is lower than the system error of 10 m/s for the fiber data, and higher than the system error for the freespace data. There are scale factor errors in the slopes that are attributed to variations from the calibration conditions. The large deviations from the linear trend are attributed to overlying fringes in the freespace data that are not correlated between the reference and signal images.

The prominent bumps in the data with widths of about 20 mm are thought to be decorrelated and offset speckles and fringes, and possibly centroid position errors in the dewarp algorithm.

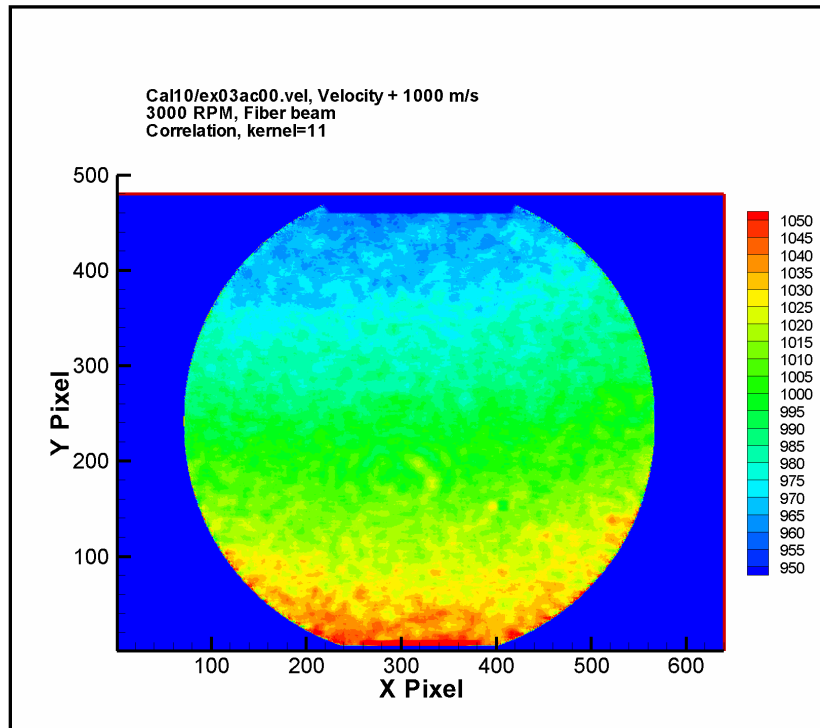


Figure 16: Single image of velocities measured for a wheel spinning at 3000 RPM. The wheel is fiber-illuminated, the reference and signal images are aligned by cross-correlation, and the ratios are smoothed by an 11x11-pixel kernel.

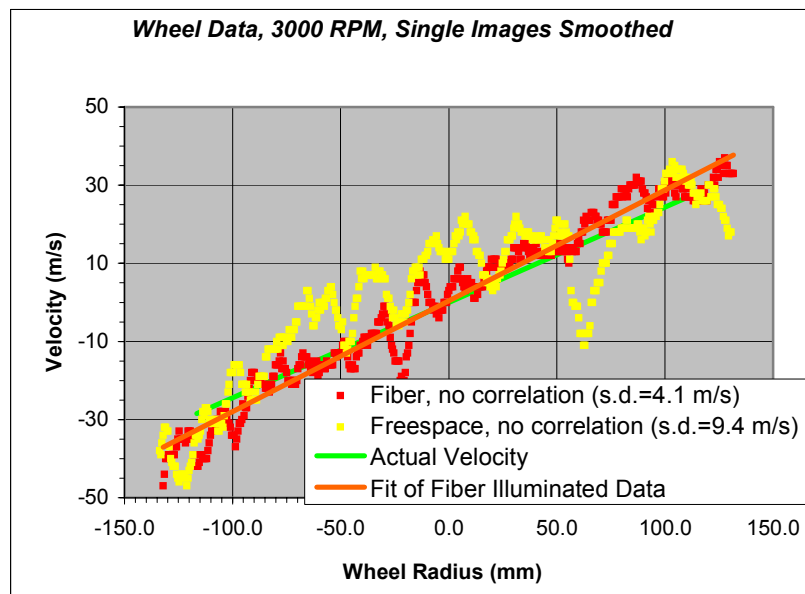


Figure 17: Vertical velocity profile across a wheel spinning at 3000 RPM. Red data indicate fiber bundle illuminated run, and the yellow data indicate freespace beam illuminated run.

The following series of graphs, Figures 18 through 21, show the effects of adding incremental improvements to the processing of the Cal10 data, whose typical speckle size is larger than the pixel pitch. The first pair of graphs, Figures 18 and 19, compare the effect of image alignment prior to taking the ratios, for single images and then averaging over ten image ratio sequences.

Figure 18 shows the difference between velocities calculated both with and without aligning the reference and signal images before taking their ratios. The plot shows vertical slices through single image ratios converted to velocities. The correlation shifts the reference image 5.7 and -5.0 pixels in the x and y dimensions, respectively. Figure 19 shows a vertical slice of ten similar velocity images averaged over time. There is a statistical improvement in scatter between the plots in Figures 18 and 19, since each image in the mean has a different speckle pattern.

Figures 20 and 21 add spatial smoothing by an 11x11 kernel to the data in Figures 18 and 19. Figure 20 is a vertical slice through a single smoothed velocity image, and Figure 21 is a ten-image average of smoothed velocity images. An improvement is clearly seen as the pixels are

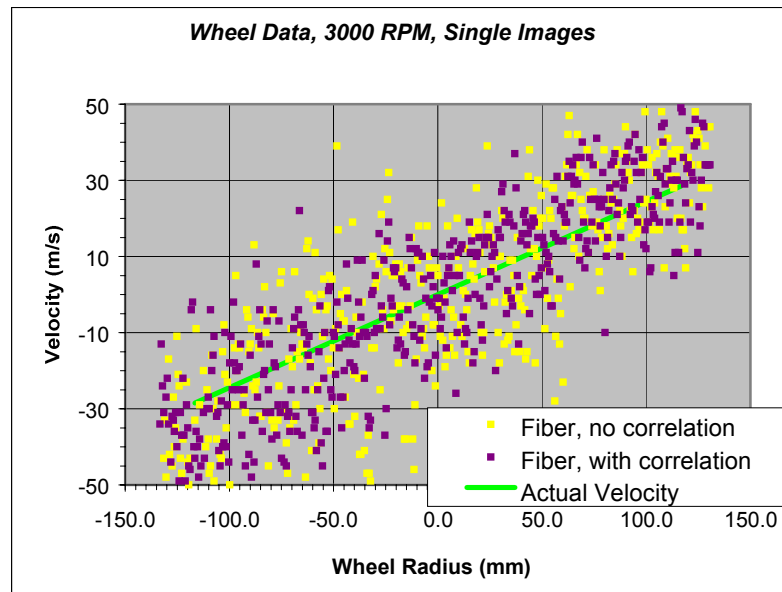


Figure 18: Single image velocity data slice, acquired using freespace beam propagation. Plots compare velocities from Signal/Reference image ratios calculated with and without alignment using 2-D cross-correlations. The high degree of scatter in the "aligned" correlated images indicate that the intensity distributions being aligned do not represent any real-space image shifts.

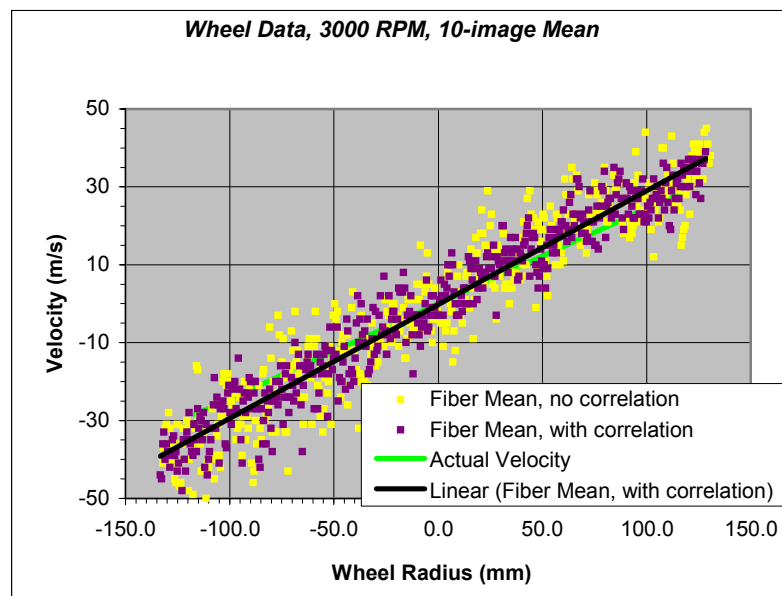


Figure 19: Velocities averaged over ten images, comparing aligned and unaligned image pairs.

averaged over time and space. There is also clear indication of partial correlation of the speckle patterns between the reference and signal images, as image alignment prior to normalization flattens some of the features in the data. The lowest standard deviation is 1.83 m/s for the correlated images spatially smoothed and averaged over time.

The calibration slope errors are consistent among the plots, and differ from the actual slope of 0.24 m/s/mm by about 17 to 23%. This slope error is due to iodine cell calibration errors caused by a linear approximation of the transmission curve and from errors reading graphically determined intercept values.

Table 1 compares the standard deviations of the data in figures 18 through. In the table, the spatial standard deviations are given for four variations of smoothing and cross-correlation. The standard deviations for both a single image and a series of ten images averaged over time show improvement from

averaging noise. The measured improvements were 54% and 55% for the unsmoothed data, and 33% and 38% for the data that were already spatially smoothed.

The average speckle size over 200 pixels in these f/4 CompA images is roughly 4 pixels/speckle, showing that an improvement is expected when spatially smoothing the data.

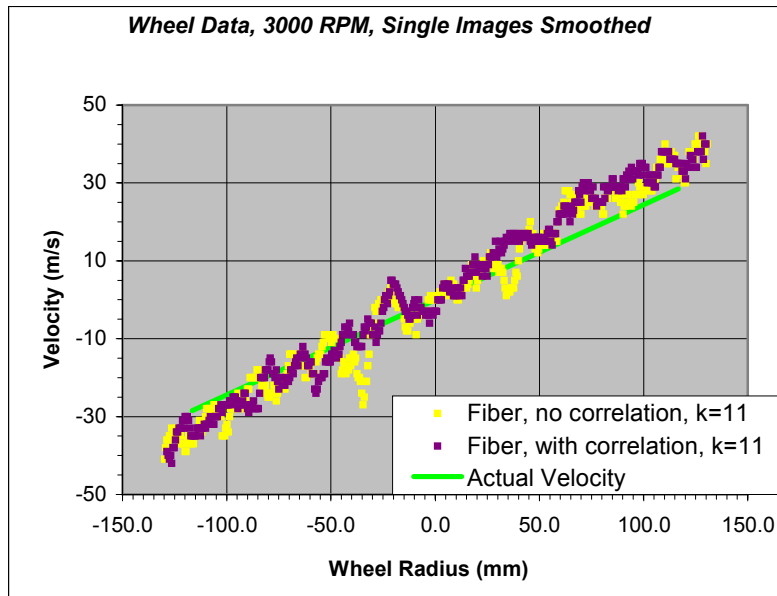


Figure 20: Velocities smoothed by an 11x11 kernel prior to taking the image ratios. The plots show both an improvement from speckle smoothing and from image alignment.

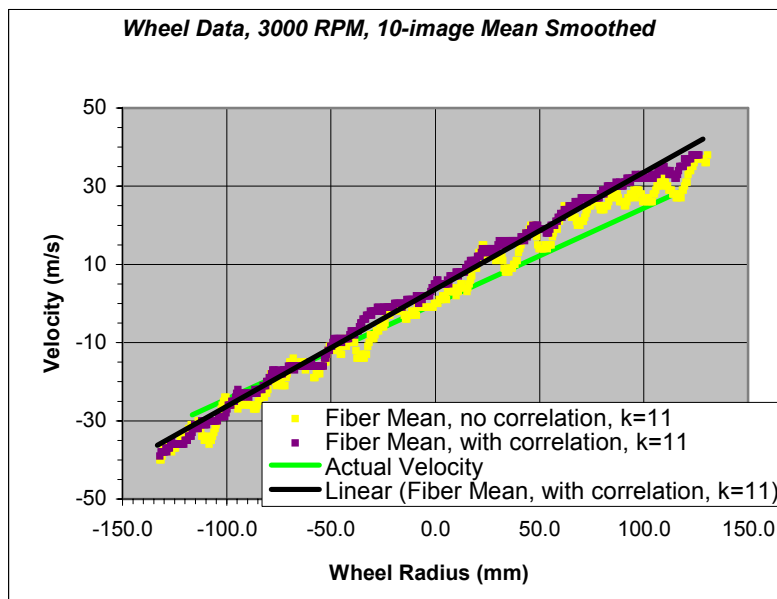


Figure 21: Velocities smoothed by an 11x11 kernel and averaged over ten velocity images. Random noise has been reduced to about 1.8 m/s.

<i>Standard Deviation Comparisons</i>			<i>s.d. (m/s)</i>
k=1	Not Correlated	Single image	17.5
		Ave image	8.07
		<i>Improvement:</i>	54%
	Correlated	Single image	12.7
		Ave image	5.76
		<i>Improvement:</i>	55%
k=11	Not Correlated	Single image	3.89
		Ave image	2.61
		<i>Improvement:</i>	33%
	Correlated	Single image	2.94
		Ave image	1.83
		<i>Improvement:</i>	38%

Table 1: Comparison of standard deviations of data in Figures 18 through 21.

LFM WAVELENGTH CORRECTION AND FIBER ILLUMINATION

The Doppler Global Velocimetry technique is based on the calibrated measurement of optical frequency (or wavelength). That is, the component image ratios are compared to a calibration between transmission ratio and optical wavelength, to assign a wavelength to each pixel in the image ratios. Any change in this wavelength from the fundamental laser wavelength is then attributed to a Doppler shift in the light scattered from the seed particles. However, the calibration is done over an average of many image pairs from a series of laser pulses, each of which varies slightly around the average wavelength (the variation is due to an active dithering of the cavity length required by the laser manufacturer to stabilize the laser). Therefore, the ability to accurately assign transmission ratios to Doppler wavelength shifts requires knowledge of the shot-to-shot laser wavelength variations; this is achieved with the Laser Frequency Monitor. So the laser wavelength is measured by the LFM and used in Equation 1 as the fundamental illumination wavelength.

A concern in the GRC development is whether, in addition to a shot-to-shot variation in the average laser wavelength, there is a spatial variation in laser wavelength (either stable or varying from shot-to-shot). Previous tests showed no conclusive evidence of a spatial variation in wavelength using the GRC Continuum laser, and data supporting this are included here. An indication of such a variation of wavelength would be a difference in distributions or statistics visible between image ratios exposed by light inside and outside the absorbing region of the I_2 curve; none were observed.

The light emitted from the fiber bundle differs from the free space beam in that the spatial correlation with the beam out of the cavity is lost due to the intentionally random coherence between the input and output ends of the fiber bundle. That is, the fiber bundle is designed to randomize the intensity distribution on the free space beam, which also randomizes any wavelength distribution. This means that any wavelength distribution might be realized as an increase in RMS variation on the image ratios taken through the attenuating region of the I_2 curve, compared to the flat field image ratios.

Figures 22 and 23 compare image ratio data of fiber bundle-delivered light illuminating a ground glass screen, taken with the laser wavelength set inside and outside the I_2 cell absorption band. The ground screen is angled slightly to cut across the beam, so that the illuminated region represents a cross-section of the laser beam stretched in the horizontal dimension.

Figure 23 is an image ratio taken inside the absorption band, at the 33% transmission point, and Figure 22 is an image ratio taken in the flat field region, with a transmission coefficient of 94%. Since the in-band transmission ratio is 33%, the color scale on Figure 23 was divided by three to provide a comparative image representing any distribution differences between the two images. The images clearly show that the expected scale taken from the transmission curve maps the zero velocity data to the flat field data very effectively. Given that the scaling was successfully achieved, any difference in distribution may be attributed to either a spatial wavelength distribution on the beam or noise.

The image ratios are masked in the same manner as Figure 7, using the thresholded reference image as the mask. Even so, the red boundaries seen on the top and bottom of the images may be considered noise, as their intensity is quite low. The red spot in

the center is a blemish on the screen and is seen as a dim region on both reference and signal images [the gray scale value of the spot is roughly 20, which is about 20% of the peak data intensity]. This artifact highlights that there can be significant correlated noise present in the raw data, where in fact the velocity is zero.

The wheel data set named Cal10 can be used to compare the fiber bundle results to the results from the beam propagating in free space. Table 2 shows

the mean, standard deviation, and noise-to-signal ratio (NSR) for various image pair ratios. In the table, data sets ff00 and ex02 are the flat field and zero velocity data for the free space beam, and ff01 and ex04 are the flat field and zero velocity data for the fiber bundle-delivered beam. Data labeled ic12 and ic18 are the image ratios shown in Figures 22 and 23. All the statistics are calculated over single image ratios, so no shot-to-shot averaging of speckle or wavelength is done. For the LFM images, the NSRs for the flat field and absorption band free space beam images are identical to two significant figures, and the NSRs for the fiber bundle images differ by 10%. A similar comparison of the

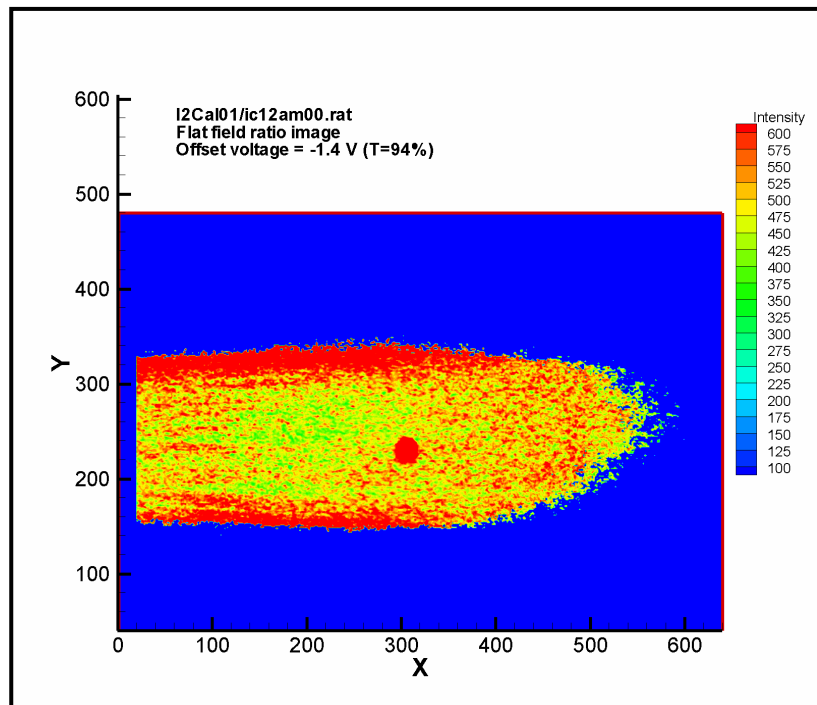


Figure 22: Flat field image ratio outside of absorption region of the iodine vapor cell. A comparison of Figures 20 & 21 shows no statistical indication of wavelength variations. Color scale is the ratio * 1000.

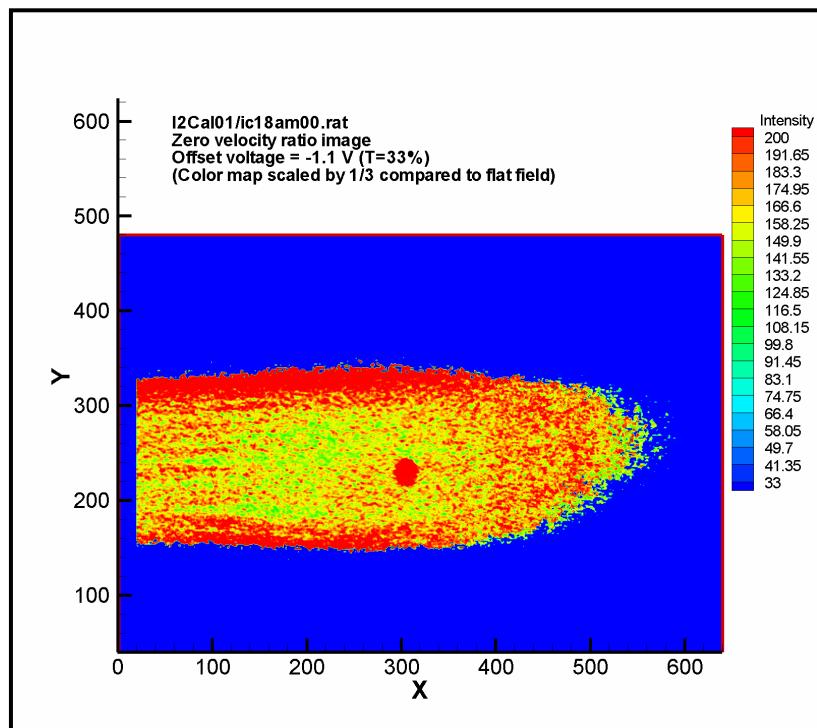


Figure 23: Zero velocity image ratio in absorption region of iodine vapor cell. Color scale is matched to flat field data.

Component A data shows the NSRs for the flat field and absorption band free space beam image ratios to differ by about 10% and 30%, respectively. Likewise, the NSRs for the I2Cal01 fiber data statistics show no trend that is attributable to a wavelength distribution. One unexplained anomaly in Table 2 is that the NSRs for the LFM are higher than for Component A; also, the LFM NSRs vary the most from run to run, whereas the Component A NSRs are quite consistent from run to run. The most likely explanation for this is a speckle size variation between the two LFM data sets; the f -numbers were used for the two runs were different, as were the image magnifications. The LFM camera lens f -numbers were $f/11$ and $f/2.4$ for the Cal10 and I2Cal01 data, respectively. Conversely, the Component A f -numbers were $f/4$ and $f/2.4$ for the two runs, but subsequent tests have suggested that the speckle sizes are smaller than the pixel size for f -numbers of $f/4$ and below. The scattering targets for both components change from 600 grit sandpaper to 200 grit ground glass between the Cal10 and the I2Cal01 runs, so this is not a differentiating factor.

To verify that the Cal10 data, in fact, were taken at the calibrated transmission regions of the I_2 curve, the LFM reference and signal image mean values were calculated and compared to the calibrated transmission ratios of the LFM iodine cell. The calibrated flat field transmission coefficient T at a seed laser offset voltage of 3.00 V is 94%, which compares well with the wheel-measured mean image ratio of 91%. Likewise, the transmission coefficients in the absorbing region with the seed laser offset voltage set to 4.12 V were 49% for both the calibrated and wheel-measured data.

CompA				LFM		
Cal10	Mean	s.d.	NSR	Mean	s.d.	NSR
ff00 (freespace)	964	110	0.11	447	186	0.42
ex02 (freespace)	421	49.4	0.12	620	261	0.42
ff01 (fiber)	604	76.9	0.13	501	163	0.33
ex04 (fiber)	283	26.9	0.10	260	78.6	0.30
I2Cal01 (fiber)						
ic12nx00 (flat field)	481	57.7	0.12	550	135	0.25
ic18nx00 (33% T)	136	20.1	0.15	262	63.3	0.24

Table 2: Mean, standard deviation, and NSR (s.d. / mean) table for single image ratios of a wheel illuminated by beams delivered either via free space propagation or fiber bundle. For each component, the NSR does not change depending on whether the wavelength is in the attenuating region or not, for either the free space or the fiber bundle cases. This suggests that, in these data, there is no detectable wavelength variation over the beam.

Fiber Bundle Illumination

The optical fiber bundle approach to delivering the laser beam to the test section is a technically viable and experimentally convenient technique. Test comparisons for the Cal10 wheel data, shown in Figure 17, show similar velocity trends but with lower noise when using the fiber bundle. No Stimulated Brillouin Scattering (SBS) power density transmission limit is observed in the power transmission through the fiber bundles.

The bundle is comprised of about 1,340 pure fused silica core multimode fibers, arranged in a random continuity between the input and output ends. The bundle ends are fused, rather than epoxied. The circular bundle ends are 8 mm in diameter, and the numerical aperture is about 0.37. Two progressively worse damage thresholds are then avoided by this approach to fiber coupling. The typical lower threshold to be avoided is burning of assembly epoxy via absorption, and the higher threshold is ablation of the glass fiber ends by an excessive power density causing thermal and acoustic shock. Eliminating the epoxy avoids the first threshold, and spreading the intensity over a large number of multimode fibers avoids the second threshold. A Teflon annulus is glued over the exposed end of the stainless steel ferrule surrounding the input end of the bundle, which protects stray light from the beam injection from ionizing and depositing metal on the face of the bundle. This bundle has been used to couple an input beam of up to 650 mJ/pulse without damage.

Figure 24 shows the ratio of transmitted power to incident power as the incident power is increased. The transmission ratio in blue is relatively constant throughout the measured range; an indication of SBS would have been for the transmitted power to be clamped at some power level, with the balance of the incident power frequency shifted and backscattered toward the laser. Jeunhomme characterizes the Brillouin-Stokes frequency shift in silica fibers, such as those in the bundle, as $-17/\lambda$, or 32 GHz, with a linewidth of $29.6/\lambda^2$, or 105 MHz, where λ is the wavelength of incident light in micrometers.⁵ Even if SBS were to occur, however, any detrimental effect would be in limiting the delivered power rather than any real spectral broadening, as the frequency shifted portion would not be transmitted to the test section.

When using the fiber delivered beam illumination, the standard LaRC cross correlation does not necessarily see enough structure in the beam to improve

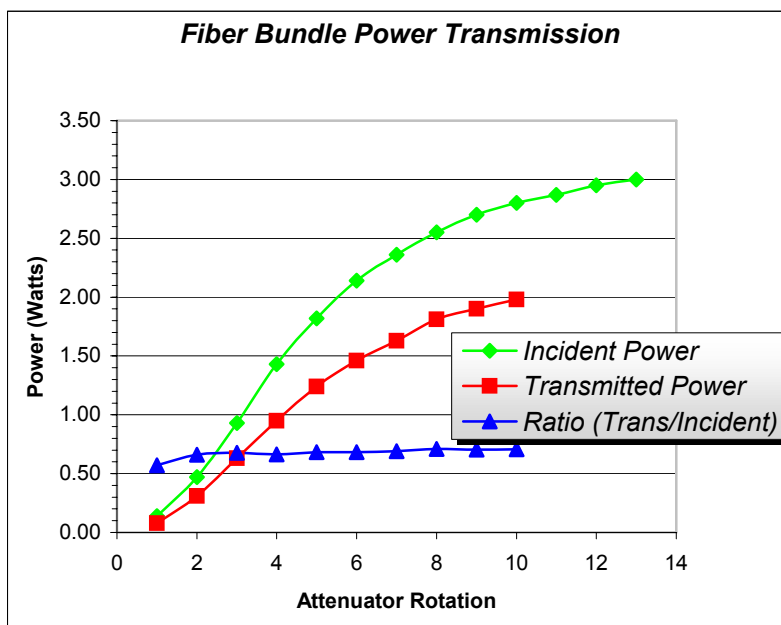


Figure 24: Fiber bundle transmission coefficient as a function of attenuator position.

alignment; in fact, it can destroy alignment and degrade the wheel measurement. Further, the cross correlation should not be needed if the dewarp process works, at least down to the pixel level of registration. Conversely, when using the freespace delivered beam illumination, the cross correlation seems to be necessary due to beam structure changes; that is, the beam fringes seem to shift between the signal and reference images. However, this fringe alignment does not necessarily represent velocity data registration, and use of it should assume that velocity gradients only occur over regions larger than the image shifts. See the Error Analysis section for more discussion.

Advantages to the fiber bundle approach are that it reduces the number of components typically needed to deliver the beam, it reduces fringe noise on the raw beam and distributes the light intensity evenly across the emitting cone, and it makes the repositioning of the measurement plane more easily automated in a test environment. Disadvantages are that it reduces the delivered light intensity by about one-third (transmits 67%) and complicates the light sheet generation when using a circular output spot. A modification specified on the output end of the next fiber being purchased will produce a more rectangular output beam. This output geometry is expected to overcome the Lagrange Invariant constraint to the sheet thickness encountered with the circular output end; while the beam divergence will be similar, the beam thickness will be potentially improved by a factor of four (2 mm width versus 8 mm diameter). The elongated output beam should also reduce the weight and complexity of the laser sheet optics, which should be important to coming field applications.

Generating a thin light sheet from the fiber bundle proved to be difficult, and believed to be caused by the LaGrange invariant and spherical aberration from the use of single element optics. Applying the LaGrange invariant to the current fiber bundle limits the theoretical sheet thickness to about 2.5 mm, assuming an output NA of 0.7 (full angle); this then is convolved with the point spread function expected from the single element, high NA optics used with the high energy laser beam to give a sheet thickness limit around 6 ± 2 mm. This number is consistent with the observed sheet thickness of around 6 to 8 mm. The Flow7 testing was done with a slit aperture at a conjugate plane in the sheet forming optics, giving a laser sheet waist of about 3 mm across. In order to eliminate the need for a slit aperture, a future fiber bundle termination with a rectangular fiber arrangement is proposed instead of a circular output termination. A reasonable bundle cross section is 2 x 50 mm. A fabrication compromise is that the output end must be epoxied rather than fused, as the jiggling to fuse the fibers is not amenable to the rectangular geometry. However, this should be acceptable, with regard to the damage threshold, as the output face is comprised of a polished, bare fiber bundle rather than an epoxied cover glass. The only remaining assembly epoxy will be between the fibers, and only after a distance in the bundle where the leakage light is fully attenuated.

SPECKLE PATTERN MINIMIZATION

The Doppler Global Velocimetry technique is based on the calibrated measurements of two wavelengths – the instantaneous base laser wavelength illuminating the flow field, and the pixel-by-pixel Doppler shifted wavelengths scattered by the seeded flow. Since the wavelengths are encoded as intensity variations using a iodine vapor absorption filter, it is clear that any difference between the reference and signal non-velocity related intensity patterns will result in a velocity error. Therefore, errors in the localized pixel velocities due to decorrelated speckle variations between the reference and signal cameras can potentially be significant.

However, proper procedures can minimize this error, either by ensuring optically that the speckle size is sufficiently smaller than the pixel size, or by digitally smoothing with a low pass kernel prior to taking the image ratios. The preferred approach is to optically reduce the speckle size by opening the camera lens apertures, as long as the depth of field is sufficiently large to reasonably cover the imaged portion of the light sheet; this approach retains the spatial resolution of the measurement. Figures 18 through 21 and Table 1 show how spatial smoothing and image series averaging reduce the effects of speckles that are larger than the pixel size.

The optical approach to reducing speckle size is opening up the camera aperture, according to the relationship described by Ennos⁶

$$\sigma \approx 1.2(1 + M)\lambda F \quad (5)$$

where σ is the diffraction-limited diameter of the speckle on the CCD array, M is the effective magnification of the lens, λ is the laser wavelength, and F is the f /number of the lens. The factor 1.2 arises due to the circular aperture symmetry, and comes from the location of the first zero in the first-order Bessel function. Note that the speckle size, or spacing, definition is somewhat arbitrary, and is only an approximation. Smith defines the noise to signal ratio (NSR) as $1/\sqrt{m}$, where m is the number of speckle correlation cells within the pixel region⁷. Then the NSR is defined as the speckle size divided by the pixel size Δx , or

$$NSR \approx \frac{1.2(1 + M)\lambda F}{\Delta x} \quad (6)$$

Table 3 and Figure 25 suggest that the speckle size is becoming sufficiently reduced at an aperture around $f/4$, for the Component A magnification used in the setup described in this report. Images were acquired over a range of lens apertures and the pixel-to-pixel noise to signal ratios were calculated at each aperture, in order to observe the point at which the NSR became independent of aperture or speckle size. In Figure 25, f -stops read off the lens were converted to f /numbers using the relation f -number = f -stop \cdot (1+ M). The correction is slight, as the magnification M in this setup is about 0.017.

Speckle2 Data Set			
<i>f</i>-stop	Mean	s.d.	NSR
f/22 (ex00)	156	54.8	0.35
f/16 (ex01)	101	31.9	0.32
f/11 (ex02)	175	49.7	0.28
f/8 (ex03)	196	46.6	0.24
f/5.6 (ex04)	77	16.5	0.21
f/4 (ex05)	62	11.4	0.18
f/2.8 (ex06)	156	27.4	0.18

Table 3: Noise to signal (NSR) for single images, calculated for a range of Component A lens apertures; statistics are calculated over 20,000 pixels. At f/4 the NSR decreases less rapidly with larger aperture, suggesting that the speckle size is close to the pixel size and pixel smoothing occurs. The *f*-number corrections use magnification $M=0.017$.

The Table 3 statistics are for the worst-case of a single image containing speckles; the image is not dewarped and is not normalized by the reference image. An analysis could also be done between the ratio of signal/reference image pairs, cross-correlated for best alignment, to the partial speckle correlation behavior described by McKenzie and Reinath.⁸ McKenzie multiplies the NSR by an experimentally-determined speckle correlation constant, with values between zero and one, that decreases the NSR when the speckle patterns in the image pairs are correlated.

Figure 25 shows the measured NSR in images as a function of lens aperture, and compares this to an image acquired at f/22 and repeatedly smoothed with a range of kernel sizes. The smoothing kernels range from 1x1 to 11x11, and have been converted to the equivalent aperture by dividing f/22 by the number of pixels smoothed in one dimension. The optical and smoothed results compare quite well over the measured range. The data in Figure 25 also compare well with the speckle NSR results published by McKenzie et al.⁸ Interestingly, the trends of these and the McKenzie results seem to flatten slightly below f/4 and above f/16. Figure 26 adds to Figure 25, on a different scale, the NSR calculated from Equation 6 in order to compare measurements to theory. The predicted values are much higher than the measured values. This may be due to differences in the parameter definitions; in fact, Smith's and McKenzie's calculations differ in that Smith uses the Ennos speckle diameter as the average spacing and McKenzie uses the Rayleigh criterion^{9,10} for resolution limit as the average speckle spacing.

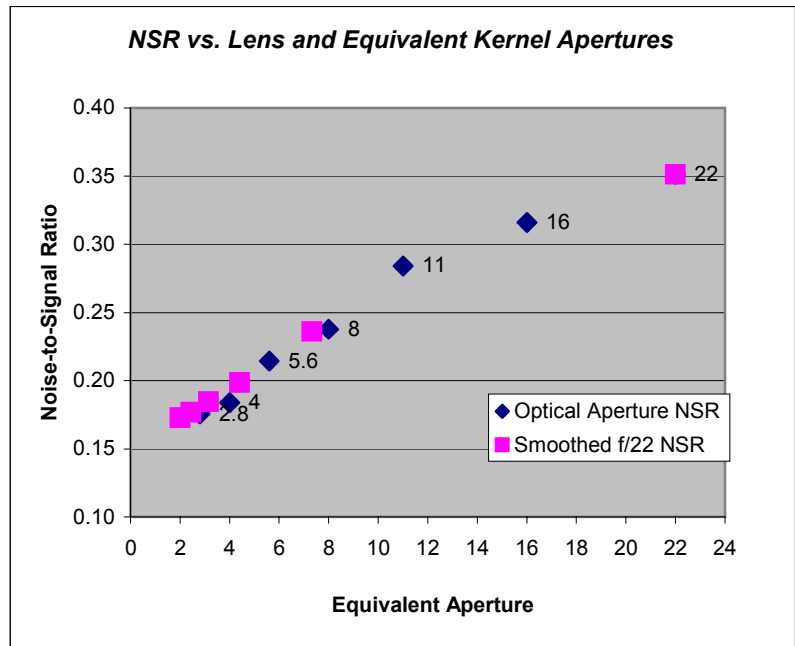


Figure 25: Plots of measured NSR over a range of lens apertures, compared to an f/22 image filtered over a range of kernel sizes. The kernel sizes are converted to equivalent apertures for ease of comparison.

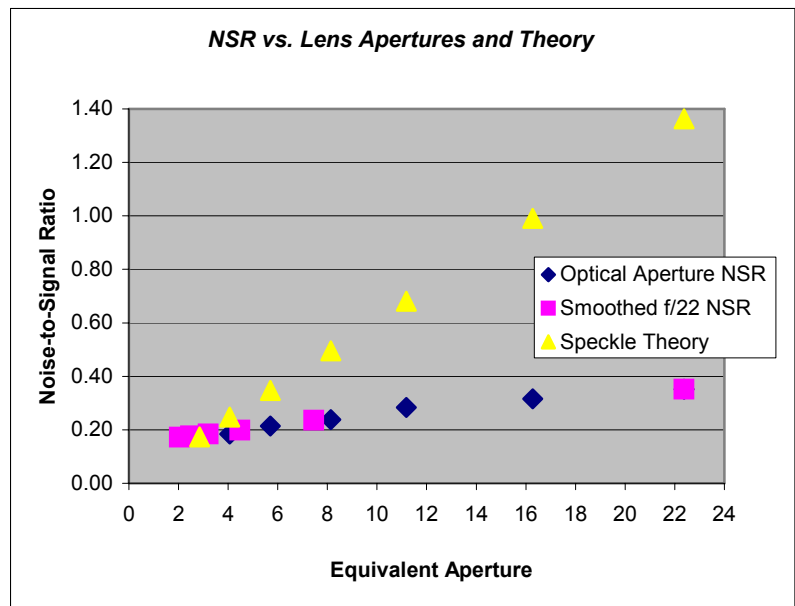


Figure 26: Adds to the data in Figure 23, on a different scale, the NSR calculated from Equation 6 in order to compare measurements to theory.

ERROR ANALYSIS

The measured data show very good correlation and agreement with the expected values, however, a repeatable slope error indicates a possible calibration error exists. A linear fit of the -1.00 V data in blue gives a slope of 1.10, a standard deviation of 7.9 m/s, an intercept of 19 m/s, and a correlation coefficient of 0.997. The largest error trend in the data appears to be an offset in the intercept. Forcing the fit through the origin alters the fit statistics, as shown in Table 4.

A similar fit of the -1.10 V data in red, excluding the three clipped data points, shows worse slopes and standard deviations. The data averaged over a larger ROI show a lower standard deviation, as expected. Table 4 shows the slope, intercept, and standard deviation for the various cases discussed above.

<i>Linear Fit Results</i>			
<i>No constraints to fit:</i>	Slope	Intercept (m/s)	S.D. (m/s)
ex00-07, core ROI	1.04	18.3	11.1
ex10-16, core ROI	1.25	-26	10.6
<i>Force fit through origin:</i>			
ex00-07, core ROI	1.10	0	11.9
ex10-16, core ROI	1.12	0	12.8

Table 4: Fit coefficients for Figure 13 plots. The regressions were calculated both with and without forcing the fit through the origin. A scale error, possibly from a calibration drift, is suspected to lead to the higher slopes.

Primary sources of random error include laser speckle decorrelation between reference and signal images, registration errors between reference and signal images, and uncertainty in the calibrations. Systematic errors include geometric errors in the optical orientations, and calibration errors in the flat field correction, measuring the transmission function, and performing the polynomial fits and interpolation of the data into the LUTs. The decorrelated speckle error is minimized by using a lens aperture of f/2.8 on both the LFM and CompA cameras.

The sensitivity of the velocities to error in various measured parameters can be described as a total differential equation of the velocity equation based on Equation 4. This can be solved for velocity U as

$$U = \frac{c\lambda_0}{R \cdot \cos\theta} \left(\frac{1}{\lambda_1} - \frac{1}{\lambda_0} \right) \quad (7)$$

so that the total differential of Equation 7, defined as

$$dU = \frac{\partial U}{\partial R} \Delta R + \frac{\partial U}{\partial \theta} \Delta \theta + \frac{\partial U}{\partial \lambda_0} \Delta \lambda_0 + \frac{\partial U}{\partial \lambda_1} \Delta \lambda_1 \quad (8)$$

becomes

$$dU = \left[\frac{-U}{R} \right] \Delta R + [U \cdot \tan \theta] \Delta \theta + \left[\frac{c}{R \lambda_1 \cos \theta} \right] \Delta \lambda_0 - \left[\frac{c \lambda_0}{R \lambda_1^2 \cos \theta} \right] \Delta \lambda_1 \quad (9)$$

Normalizing this by velocity, we get

$$\frac{dU}{U} = \left[\frac{-\Delta R}{R} \right] + [\Delta \theta \cdot \tan \theta] + \left[\frac{\Delta \lambda_0}{\lambda_0 - \lambda_1} \right] - \left[\frac{\lambda_0 \Delta \lambda_1}{\lambda_1 (\lambda_0 - \lambda_1)} \right]. \quad (10)$$

In the equations, U is the Doppler velocity component measured, R is the magnitude of the vector difference $\mathbf{a}-\mathbf{l}$, θ is the included angle between R and the flow direction, and λ_0 and λ_1 are the base laser wavelength and Doppler shifted wavelengths, respectively. Equation 9 then shows the contribution of velocity error for given errors in parameters R , θ , λ_0 , and λ_1 . Representative values for these parameters are discussed below.

The geometrical uncertainties are estimated from angular errors in aligning the light sheet, Component A head, and flow nozzle axis. Each of these uncertainties is estimated to be $\pm 2^\circ$, which lead to uncertainties in R and θ of ± 0.06 and $\pm 2^\circ$. Although these uncertainties could certainly be reduced further in subsequent setups, they do represent the current setup and what are believed to be typical field based setup uncertainties. Note that the first two terms in Equation 9 are proportional to U (geometrical errors) and the last two are absolute errors. These absolute wavelength errors are the crux of the art of the measurement technique, and are where most of the potential pitfalls in the technique lie.

Conversely, the form of Equation 10 highlights that the velocity uncertainty due to the error in measuring the wavelengths decreases with higher velocity; the proportional errors in R and θ are systematic, and can be reduced readily. The following error estimate includes the aforementioned parametric errors, but does not include errors in the signal/reference ratios due to decorrelated speckle patterns.

Substituting the values and uncertainties from Table 3 into Equation 9 leads to

$$dU = \pm 0.09U \pm 10 \text{ m/s} \quad (11)$$

and

$$dU_{RMS} = \pm 0.06U \pm 7 \text{ m/s} \quad (12)$$

The total differential dU gives a worst-case estimate, and the RMS result dU_{RMS} takes into account that the errors are not always additive. These results are summarized in Table 5.

Parameter	Value	Uncertainty
R	1.09	0.06
θ	0°	±2°
λ_0	532.19888 nm	±10 ⁻⁵ nm
λ_1	532.19888 nm	±10 ⁻⁵ nm
Velocity Error	±10 m/s	±9%

Table 5: Error estimates for parameters in the velocity equation. Does not include decorrelated speckle modulation error.

The largest contribution to the scale error is the angular positioning of the light sheet and the Component head; the coincidence of the flow axis with the component's sensitive axis is relatively insensitive. The precision of most of the values reported herein is based on the estimated precision of the gray scale values from which they stem.

Possible Wavelength Calibration Errors:

- A possible reason for the slope errors in the pressure ratio trends is in the calibration data. Looking at the LFM data here, in order to eliminate Doppler effects due to flow a comparison was made between LFM transmission ratios from the calibration run and the Flow7 run. If the calibration data are accurate during the run, then it seems that the following relationship should be observed between the mean ratio values:

$$\frac{ic12dx_{ROIave}}{ic20dx_{ROIave}} = \frac{ff00dx_{ROIave}}{ex00dx_{ROIave}} \quad (11)$$

where the constants $ic12dx$ and $ic20dx$ are averages (temporal, then over the ROI) of image ratios at seed laser offset voltages -1.40 V and -1.00 V (recorded during the calibration run), and $ff00dx$ and $ex00dx$ are the corresponding flat field and velocity averages (recorded during the velocity run). That is, $ic12$ and $ff00$ data are both taken at seed laser offset voltages of -1.40 V, and $ic20$ and $ex00$ are both taken at seed laser offset voltages of -1.00 V. The actual values for the relationships in Equation 11 are 5.6 and 17, which differ by a factor of three.

The wavelength correction algorithm automatically corrects part of this discrepancy, by using the flat field data to normalize the peak transmission; however, a correction is not done to the minimum in the transmission curve, so there would still remain an error in slope in the calibration curve.

Therefore, there is thought to remain a small scale factor error in the LFM wavelength calibration LUT, and, presumably, a similar calibration error remains in the CompA LUT. While the magnitude of this error is not yet known, it appears to be less than the 9% geometric error, when comparing the measured slope error to known slope uncertainties.

- Divide-by-zero errors were avoided algorithmically by setting reference pixel values of zero to one before the ratio step; if this happens to divide, say, a zero or one in the signal image, the result is a large ratio (high velocity) when in fact the signal levels were merely in the noise. This is compensated for by the thresholding procedure shown later in this report, but could be improved at this wavelength calculation stage instead.
- Calibration image pairs are not dewarped as in the velocity data. Rather, a spatial correlation is performed. The reasoning was that only a spatial average would be used in the calibration, but a better approach would be to low pass filter (to a resolution below that of any warping shifts) before taking the ratios, and then perform the temporal and spatial averages.

Calculated Velocity Error

The accuracy of the pressure gauge was calibrated after the data acquisition to be ± 0.2 psia, and the resolution was observed to be about ± 0.01 psia. Based on the accuracy, the pressure data is recorded with three significant figures, which gives a resolution comparable to the Mach table resolution.

The proportional error was measured to be about 0.3%. The calculated Mach number table resolution is 0.01, or about 3 m/s. Therefore, the baseline errors in the calculated velocities are estimated to be around 4 m/s absolute error plus a proportional error of 0.3%.

However, a possible cause for the deviation from linear of the velocity data in Figure 13 is explained by verified pressure leaks in the tap from the nozzle plenum. Such leaks occurring above some minimum pressure could indicate lower core velocities than actually measured at the higher pressures, which is consistent with the measured velocities. There are two splices and four couplings in the tubing between the tap and the gauge.

Speckle Related Error

The use of the correlation approach to improve pixel registration deserves close inspection. It is important to consider that every test situation can produce images with more or less sensitivity to speckle effects. However, in general, the images in each component head can be thought of as a superposition of an image intensity distribution and a speckle/fringe pattern. The typical approach to implementing subpixel registration is to perform a bulk image cross-correlation between each dewarped reference and signal image, possibly in two stages (course and fine shifts), and then shift the signal image by the two-dimensional displacement indicated by the correlation peak position.

The LaRC software calculates the average shift over the image series, which should have the effect of reducing the speckle sensitivity. The cross-correlation approach finds the largest pixel-by-pixel integrated product over a range of shifts between the two intensity patterns. This approach has shown improvement in the RMS deviations across an image ratio, but it is believed to be due, at least in part, to speckle field alignment rather than real image registration. While that may reduce RMS variations, it does not improve the accuracy of the velocity contribution to the intensity measurements when the velocity varies spatially over a region smaller than the shift amount.

Consider that each camera image is a real image of the test location modulated by a speckle pattern formed by the aperture of the camera lens (while other apertures do exist in the optical system, the lens aperture is the dominant one determining the speckle statistics in the standard application). The Doppler encoded velocity information is indisputably correlated to the image location from where the light was scattered, in both the reference and signal cameras; the goal is to have each of these scattering image points as closely registered as possible between the reference and signal images. However, the speckle pattern modulating each image is a interference effect subject to global and local phase objects in the imaging paths to which the image positions are not susceptible. Therefore, it is reasonable that an intensity distribution on the CCD arrays may have independent components from physical objects and speckle patterns.

The degree to which the speckle pattern correlation dominates the real image correlation is a function of the degree of correlation between the two speckle patterns in the reference and signal images. When the speckle patterns are highly correlated, the calculated peak image shift position may be entirely due to the speckle pattern. In the case of extreme decorrelation between the speckle patterns, the contribution of the real image to the shift position will increase relative to the speckle pattern contribution. However, even in the case where the speckle patterns are decorrelated, there will be a clear correlation peak representing the best alignment of the decorrelated speckle patterns, since the imaging parameters defining the average speckle sizes present in the distributions are the same.

Two aspects of the image data can be used to judge the possibility of speckle-induced misalignment: 1. if spatial velocity variations in the image are on a length scale larger than the speckle pattern shifts, then the correlation shifts should on average improve the image ratio accuracy; an alternative way of characterizing this is to test for when the noise from speckle mismatch exceeds that from other random errors (that is, aligning the images or velocities may add more random noise by misregistering speckles; 2. when real image contrast dominates speckle contrast.

However, the preceding dewarping process relies on dots having vague boundaries. That is, it is expected that the dewarping process actually introduces localized distortion errors with magnitude of 1-3 pixels, while the subsequent bulk image shift only repairs a net global fraction of this. The speckle mottling seen on the GRC data may be due to mis-registered pixel normalization due to residual local distortions. It may also be due

to the two speckle patterns (Reference and Signal) being uncorrelated to some degree. An analyses on speckle decorrelation is done by McKenzie,⁸ and uncertainty estimates due to pixel registration is done by Morrison and Gaharan.¹¹

A preferable alternative to the current cross-correlation approach is proposed for test situations where spatial resolution of the velocity is smaller than the speckle-induced shift. The images can be aligned manually by physical features in the images, such as bright seed particles and rigid fixtures in the setup. It may be beneficial to enhance the contrast of the alignment images to bring out poorly illuminated fixtures. It could also be beneficial to add an appropriate target in the camera field of view during the test, expressly for registering the images. These approaches would best be combined with the maximum optical speckle reduction allowable by the test hardware.

CONCLUSIONS

Many incremental improvements have been integrated into the data acquisition and processing procedures for the DGV measurements at GRC. As is typical, most of these techniques and procedures go well beyond the level of detail reported in the literature, and represent a significant advancement in the learning curve needed to successfully implement the DGV technique in facilities at GRC.

The velocity distributions and trends agree well with those expected from the flow that was generated, with deviations close to those expected from the error analysis. The images show the velocity distributions clearly, and the core region is discernable in both the 2-D image maps and the row slices taken at each pressure distribution. An improvement in future testing would be to seed the ambient air to better discern the outer flow boundaries.

The slope, and offset errors indicate that a calibration adjustment, possibly of either the velocity measurement or the pressure ratio measurement, may improve the data. It is not yet clear whether these residual errors are due to the velocity calculation algorithm, a frequency calibration drift, or leaks in the pressure tap. Even so, the agreement with expected error indicates that the procedures and data are credible and realistic.

The slopes given by the core velocity comparisons with calculated velocities are about 10% higher than expected, but have very good correlations with fits to a linear equation ($R > 0.996$); therefore, the slope error is thought to be a calibration error or other systematic error. The offset errors in the trend are around the absolute error of 10 m/s expected in the technique. Again, since this does not appear to be a random error from test run to test run, it may be correctable as the calibration is refined.

The LFM corrections show no need for a spatially resolved wavelength correction for either the free space beam or fiber bundle beam delivery techniques. Ratio images for both beam delivery techniques comparing flat field data and attenuation region data show neither meaningful spatial distributions nor statistical differences between the two wavelength-discriminated cases. While other lasers may have shown a spatial distribution, or there may actually be a very low-level distribution on the GRC Continuum laser, there are two reasons a wavelength distribution does not need to be measured at GRC: 1. any distribution is below the noise floor of the current hardware; 2. the fiber bundle would spatially flatten any distribution in the same way it flattens the intensity distribution, which would tend to desensitize the measurements rather than add error.

The optical fiber bundle approach to delivering the laser beam to the test section is a technically viable and experimentally convenient technique. Test comparisons with freespace beam propagation data show similar velocity trends but with lower noise when using the fiber bundle. No Stimulated Brillouin Scattering threshold is observed in the power transmission through the fiber bundles.

When using the fiber delivered beam illumination, the standard LaRC cross correlation does not necessarily see enough structure in the beam to improve alignment; care should be taken to understand why any image shifts are implemented. When using the freespace delivered beam illumination of a wheel, the cross correlation seems to be necessary due to beam structure changes; that is, the beam fringes seem

to shift between the signal and reference images. However, this fringe alignment does not necessarily represent velocity data registration, and should assume velocity gradients only occur over regions larger than the image shifts (this requirement proves to be true for the wheel data).

Advantages to the fiber bundle approach are that it reduces the number of components typically needed to deliver the beam, it reduces fringe noise on the raw beam and distributes the light intensity evenly across the emitting cone, and it makes the repositioning of the measurement plane more easily automated in a test environment. Disadvantages are that it reduces the delivered light intensity by about one-third (transmits 67%) and complicates the light sheet generation when using a circular output spot. An elongated output profile is preferable, and will be incorporated into the next flow testing phase.

The transition from wheel measurements to flow measurements required very different approaches to both acquisition and processing. Signal level complications encountered with the wheel tests became intolerable with the greater dynamic range required of the supersonic flow tests; while the scattering cross-section in the former case didn't change as a function of wheel velocity, it did indeed change with velocity in the latter case that used an aerosol to seed the flow. As the flow increased, the seed density decreased and the signal level dropped. At the same time, the greater red-shift induced in the scattered light caused greater attenuation by the iodine vapor, further reducing the signal level. In addition to these practical issues, a software conflict in the data acquisition code had the effect of recording lower gray scale values than are observed using the monitoring software during the signal level adjustments. Once these issues were found, they were corrected for in subsequent tests. The processing software used for wheel data and flow data are also very different, due to differences in the image geometry and an improvement to the laser frequency correction approach used for the flow data processing.

The absolute frequency conversion approach required a procedural change that greatly increased the accuracy of the calibration between intensity ratios and optical wavelength. The approach was driven by the large range of Doppler shifts typical of high speed flow measurements, and required a constant split between the reference and signal cameras between performance of the iodine cell calibration and the velocity data collection procedures. In addition, a non-linear mapping of the absorption curve is required to avoid large errors at the endpoints of the curve. The initial processing approach corrected for a variable ratio, in contrast to the traditional single-point flat field procedure that only corrects for an offset, not a scale factor in the calibration. The approach was changed to the traditional absolute wavelength measurement technique, however, which uses an intensity-to-wavelength look-up-table to improve accuracy and to extend the Doppler shift band to the non-linear regions of the absorption line. This improvement had the side effect of slightly reducing the dynamic range previously available, as the fine exposure adjustment built into the system to maximize the signal in each camera for each test could no longer be used (it has been observed that the ideal flat field ratio split is not necessarily constant during the time between the calibration and the velocity data acquisition, possibly due to polarization sensitivity). However, this was more than compensated for by the increased accuracy of the data near the flatter endpoints of the iodine absorption line. It is believed that a multi-point

flat field correction can be developed to better correct the non-linear absorption curve at the time of the test (e.g. measure both endpoints of the absorption line rather than just the transmission peak, to fit both the scale and offsets to the I_2 cell characterization). Refer to the Error Analysis section for more discussion on this topic.

REFERENCES

1. Yeh, Y., Cummins, H., "Localized Fluid Flow Measurements with a He-Ne Laser Spectrometer," *Applied Physics Letters*, Vol. 4, No. 99, 1964, pp. 176–178.
2. Komine, H., Brosnan, S., Litton, A.B., Stappaerts, E.A., "Real-Time Doppler Global Velocimetry," AIAA 29th Aerospace Sciences Meeting, Reno, NV, AIAA 91-0337, Jan. 1991.
3. "Equations, Tables, and Charts for Compressible Flow," NASA Ames Research Center Staff, 1953.
4. Clancy, P.S., Samimy, M., "Two-Component Planar Doppler Velocimetry in High Speed Flows," *AIAA Journal* Vol.35, No. 11, November 1997.
5. Jeunhomme, L.B., "Single-mode Fiber Optics, Principles and Applications," 2nd Edition, Marcel Dekker, Inc., 1990, pp. 324–325.
6. Ennos, A.E., "Speckle Interferometry," in *Topics in Applied Physics*, Vol. 9, "Laser Speckle and Related Phenomena," J.C. Dainty, ed., Springer-Verlag, 1975, p. 207.
7. Smith, M.W., "The Reduction of Laser Speckle Noise in Planar Doppler Velocimetry Systems," 20th AIAA Advanced Measurement and Ground Testing Technology Conference, 15–18 June 1998, Albuquerque, NM, AIAA 98-2607.
8. McKenzie, R.L., Reinath, M.S., "Planar Doppler Velocimetry Capabilities at Low Speeds and Its Application to a Full-Scale Rotor Flow (Invited)," 21st AIAA Aerodynamic Measurement Technology and Ground Testing Conference, 19–22 June 2000, Denver, CO, AIAA 2000-2292.
9. Born, M., Wolf, E., "Principles of Optics," 6th Edition, Peramon Press, 1980, p. 333.
10. Hecht, E., "Optics," 3rd Edition, Addison Wesley Longman, Inc., 1998, pp. 461–465.
11. Morrison, G.L., Gaharan, C.A. Jr., "Uncertainty Estimates in DGV Systems Due to Pixel Location and Velocity Gradients," *Meas. Sci. Technol.* **12** (2001) 369–377.

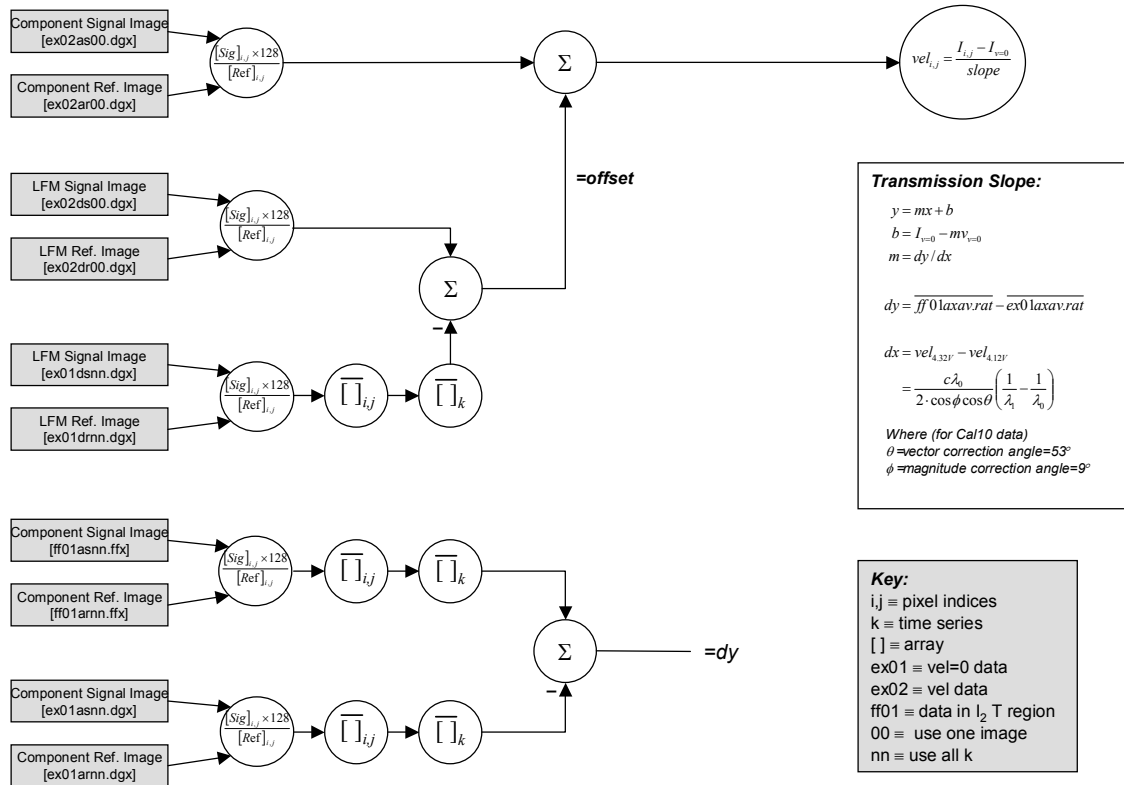
APPENDIX—DIFFERENTIAL VELOCITY PROCESSING

Two velocity processing approaches were developed for the GRC DGV system; one is a differential frequency conversion and the other is an absolute frequency conversion. The differential velocity processing approach used for the narrow-band wheel data relies on a linear approximation of the desired region of the iodine absorption curve. It relies on a differential LFM correction and a two-point normalization of the iodine absorption curve. The differential technique is described below, and the absolute technique is described in the body of the CR.

The differential approach corrects both endpoints of the calibration curve to the test data values, using the flat field and the zero velocity ratio averages. The LFM correction to each velocity image ratio is then a normalized offset from the CompA ratio, rather than an absolute frequency measurement. While this technique is not usually more accurate than a more direct absolute frequency measurement, it allows for intensity drifts in the absorption curves prior to the velocity data acquisition. The absolute approach assumes that the calibration curve represents the current image ratio split between the components cameras, and is potentially more accurate since it uses interpolation of a high order fit LUT, rather than a linear approximation currently used in the differential approach.

The following diagram is a schematic representation of the differential approach.

GRC DGV Velocity Processing Procedure Differential Linear Approximation



CTL - 3/14/02

Wheel Calibration: (Use 0 m/s velocity intensity.)

Follows the above state diagram and assumes the following data have been acquired:

- Dot card images of Components A and D
- Flat field images in transmitting region of iodine cell; also record seed laser voltage
- Velocity images with wheel RPM=0 (or very slowly rotating); also record seed laser voltage set to mid-point of transmission line
- Velocity images at full wheel speed, with seed laser voltage at 1/2 transmission point.

Process data by the following steps:

1. Modify raw *.dtr images to increase contrast and brighten background:
 - a. Import image into ImageTool
 - b. Click "show Contrast Control" button – drag contrast bar up until dot field looks good...
 - c. Copy image to clipboard; paste into Photoshop.
 - d. Click on foreground selector; pick color between dots with eyedropper.

- e. Select with “magic wand” the dark background which will be converted to the picked color; change background color by selecting paint bucket and clicking on selected region.
 - f. Save as raw file & exit; rename raw file to *.dtr.
2. Process all LFM and CompA data through *Wheel03*, to get dewarped, low-passed, and aligned 16-bit Reference & Signal images. Check whether the alignment gives image feature registration or speckle pattern registration.
3. Ratio LFM and CompA Ref & Signal image pairs using *DGVratio16.exe*.
4. Calculate mean pixel value of the mean LFM and CompA ratio images using *ImageStats_mean16.exe*. [*ImageStats_mean16* also generates statistics for one image as a byproduct; if run for a single image, mean and s.d. over the image are stored in a text file and printed to the CRT.] That is, calculate the mean over i,j and then over k. Every subsequent zero velocity CompA image mean should have the same offset to its LFM mean [tests show an actual variation of 3-4 pixel values – see notes 2/14/02]. Therefore, every non-zero velocity CompA ratio pixel should be offset by the offset found here.
5. Cal10/ex04a mean, mean from step 4 can be used as the zero-velocity value (process through programs: *DGVratio16* and *ImageStats_mean16* (can use appropriate versions of *dgvratio16.bat* and *Stats.bat*).
6. Process Cal10/ff01a & d as in step 5: *DGVratio16* and *ImageStats_mean16* [1st call to *ImageStats_mean16* prints mean to the CRT]. [This gives the gray scale value at the flat field point, corresponding to the graphically-determined velocity.]
7. Compute linear equation for I vs. λ ... [from calibration steps 5 & 6 above]:
 $y = mx + b$, where $m = dy/dx = [\text{FlatFieldA.rat}_{\text{mean,mean}} - \text{ZeroVelA}_{\text{mean,mean}}] /$
Corresponding velocity in gray levels / m/s, and $b = 301 - 2.021 * 0$. Enter slope and intercept into last two parameters of each velocity data set's *vela.set* file.

Velocity Calculation: (Use 3000 RPM data.)

1. Take 3000 RPM data as per LaRC procedure.
2. Process LFM and CompA data through *Wheel03*, to get dewarped, low-passed, and aligned 16-bit Reference & Signal images.
3. Ratio LFM and CompA Ref & Signal image pairs.
4. Calculate mean pixel value of the LFM and CompA ratio images using *ImageStats16*.
5. Compute intensity offset of CompA (ex03a) pixel values from LFM (ex03d) pixel values. (offset, since $\Delta\lambda$ shifts the transmission curve.) Use this relationship:

$$\text{CompA}_{\text{nn.rat}}^{\text{v-corrected}} = 500 + \text{ex03a}_{\text{nn.rat}} + [\text{ex03d}_{\text{nn.rat}}^{\text{mean}} - \text{ex04d.rat}_{\text{mean,mean}}]$$

where values are offset by 500 to avoid negative numbers

Enter $\text{ZeroVelocityD.rat}_{\text{mean,mean}}$ into each velocity data set's *freqa.set* file; run *freqa.bat*.

These are now arrays of pixel intensities corrected for laser intensity and frequency variations. They now need to be converted to velocity by using step 6.

6. Run each I- and λ -corrected CompA image through program *Intensity_to_Velocity.exe* to convert gray levels to velocities in m/s (run *vela.bat*).

The above steps are condensed into batch files or called as DOS commands. An example using Cal10 data sets follows (after processing through LaRC routines wheel01, wheel02, and wheel03):

- d:\dgvprocessing\cal10\dgvratio_ex04a.bat
 - d:\dgvprocessing\cal10\dgvratio_ex04d.bat
 - d:\dgvprocessing\cal10\dgvratio_ex03a.bat
 - d:\dgvprocessing\cal10\dgvratio_ex03d.bat
 - d:\dgvprocessing\cal10\dgvratio_ff01a.bat
 - d:\dgvprocessing\cal10\dgvratio_ff01d.bat
 - d:\dgvprocessing\ImageStats_mean16.exe
d:\dgvprocessing\cal10\statsratio_ex04d.set
 - d:\dgvprocessing\ImageStats_mean16.exe
d:\dgvprocessing\cal10\statsratio_ex04a.set
 - d:\dgvprocessing\ImageStats_mean16.exe
d:\dgvprocessing\cal10\statsratio_ff01a.set
 - d:\dgvprocessing\Freq_correction.exe d:\dgvprocessing\Cal10\ex03\freqa.set
 - d:\dgvprocessing\Intensity_to_Velocity.exe d:\dgvprocessing\Cal10\ex03\vela.set
- (Note: these iconized programs can be called in Windows98 by dragging the appropriate set file onto them.)

File name conventions:

xnn.rat => raw ratio image in /raw directory
cnn.rat => freq-corrected raw ratio image in /frq directory
cnn.vel => cnn.rat converted to raw velocities in /vel directory
vnn.tif => cnn.rat converted to TIF velocity image in /vel directory

Mean => image array series averaged over each pixel's time series; output is an average array

Mean,mean => spatial average of a single average array; output is a single mean and standard deviation.

REPORT DOCUMENTATION PAGE			Form Approved OMB No. 0704-0188	
Public reporting burden for this collection of information is estimated to average 1 hour per response, including the time for reviewing instructions, searching existing data sources, gathering and maintaining the data needed, and completing and reviewing the collection of information. Send comments regarding this burden estimate or any other aspect of this collection of information, including suggestions for reducing this burden, to Washington Headquarters Services, Directorate for Information Operations and Reports, 1215 Jefferson Davis Highway, Suite 1204, Arlington, VA 22202-4302, and to the Office of Management and Budget, Paperwork Reduction Project (0704-0188), Washington, DC 20503.				
1. AGENCY USE ONLY (Leave blank)		2. REPORT DATE February 2003		3. REPORT TYPE AND DATES COVERED Final Contractor Report
4. TITLE AND SUBTITLE Doppler Global Velocimetry at NASA Glenn Research Center: System Discussion and Results			5. FUNDING NUMBERS WBS-22-708-73-26 NCC3-861	
6. AUTHOR(S) Christian T. Lant				
7. PERFORMING ORGANIZATION NAME(S) AND ADDRESS(ES) Ohio Aerospace Institute 22800 Cedar Point Road Brook Park, Ohio 44142			8. PERFORMING ORGANIZATION REPORT NUMBER E-13780	
9. SPONSORING/MONITORING AGENCY NAME(S) AND ADDRESS(ES) National Aeronautics and Space Administration Washington, DC 20546-0001			10. SPONSORING/MONITORING AGENCY REPORT NUMBER NASA CR-2003-212179	
11. SUPPLEMENTARY NOTES Project Manager, Mark P. Wernet, Optical Instrumentation Technology Branch, NASA Glenn Research Center, organization code 5520, 216-433-3752.				
12a. DISTRIBUTION/AVAILABILITY STATEMENT Unclassified - Unlimited Subject Category: 35 Available electronically at http://gltrs.grc.nasa.gov This publication is available from the NASA Center for AeroSpace Information, 301-621-0390.			12b. DISTRIBUTION CODE	
13. ABSTRACT (Maximum 200 words) A ruggedized Doppler Global Velocimetry system has been built and tested at NASA Glenn Research Center. One component of planar velocity measurements of subsonic and supersonic flows from an under-expanded free jet are reported, which agree well with predicted values. An error analysis evaluates geometric and spectral error terms, and characterizes speckle noise in isotropic data. A multimode, fused fiber optic bundle is demonstrated to couple up to 650 mJ/pulse of laser light without burning or fiber ablation, and without evidence of Stimulated Brillouin Scattering or other spectral-broadening problems. Comparisons are made between spinning wheel data using illumination by freespace beam propagation and fiber optic beam delivery. The fiber bundle illumination is found to provide more spatially even and stable illumination than is typically available from pulsed Nd:YAG laser beams. The fiber bundle beam delivery is also a step toward making remote measurements and automatic real-time plume sectioning feasible in wind tunnel environments.				
14. SUBJECT TERMS Doppler Global Velocimetry; Planar Doppler Velocimetry; Supersonic velocity measurement; Fiber optic laser beam delivery			15. NUMBER OF PAGES 51	
			16. PRICE CODE	
17. SECURITY CLASSIFICATION OF REPORT Unclassified	18. SECURITY CLASSIFICATION OF THIS PAGE Unclassified	19. SECURITY CLASSIFICATION OF ABSTRACT Unclassified	20. LIMITATION OF ABSTRACT	